ABSTRACT

Title of dissertation: Microfabricated Bulk Piezoelectric Transformers

Oliver M. Barham, Doctor of Philosophy, 2017

Dissertation directed by: Professor Don DeVoe
Department of Mechanical Engineering

Piezoelectric voltage transformers (PTs) can be used to transform an input voltage into a different, required output voltage needed in electronic and electromechanical systems, among other varied uses. On the macro scale, they have been commercialized in electronics powering consumer laptop liquid crystal displays, and compete with an older, more prevalent technology, inductive electromagnetic voltage transformers (EMTs). The present work investigates PTs on smaller size scales that are currently in the academic research sphere, with an eye towards applications including micro-robotics and other small-scale electronic and electromechanical systems. PTs and EMTs are compared on the basis of power and energy density, with PTs trending towards higher values of power and energy density, comparatively, indicating their suitability for small-scale systems. Among PT topologies, bulk disc-type PTs, operating in their fundamental radial extension mode, and free-free beam PTs, operating in their fundamental length extensional mode, are good candidates for microfabrication and are considered here. Analytical modeling based on the Extended Hamilton Method is used to predict device performance and integrate

mechanical tethering as a boundary condition. This model differs from previous PT models in that the electric enthalpy is used to derive constituent equations of motion with Hamilton's Method, and therefore this approach is also more generally applicable to other piezoelectric systems outside of the present work. Prototype devices are microfabricated using a two mask process consisting of traditional photolithography combined with micropowder blasting, and are tested with various output electrical loads. 4mm diameter tethered disc PTs on the order of .002cm^3, two orders smaller than the bulk PT literature, had the following performance: a prototype with electrode area ratio (input area / output area) = 1 had peak gain of 2.3 ($\pm$ 0.1), efficiency of 33 ($\pm$ 0.1)% and output power density of 51.3 ($\pm$ 4.0)W cm^{-3} (for output power of 80 ($\pm$ 6)mW) at 1MΩ load, for an input voltage range of 3V-6V ($\pm$ one standard deviation). The gain results are similar to those of several much larger bulk devices in the literature, but the efficiencies of the present devices are lower. Rectangular topology, free-free beam devices were also microfabricated across 3 orders of scale by volume, with the smallest device on the order of .00002cm^3. These devices exhibited higher quality factors and efficiencies, in some cases, compared to circular devices, but lower peak gain (by roughly $\frac{1}{2}$). Limitations of the microfabrication process are determined, and future work is proposed. Overall, the devices fabricated in the present work show promise for integration into small-scale engineered systems, but improvements can be made in efficiency, and potentially voltage gain, depending on the application.

Microfabricated Bulk Piezoelectric Transformers

by

Oliver M. Barham

Dissertation submitted to the Faculty of the Graduate School of the
University of Maryland, College Park in partial fulfillment
of the requirements for the degree of
Doctor of Philosophy
2017

Advisory Committee:
Professor Don DeVoe, Chair/Advisor
Professor Alireza Khaligh, Dean's Representative
Professor Abhijit Dasgupta
Professor Amr Baz
Professor Sarah Bergbreiter

Dedication

To my parents, Čelica Milovanović, Byzantine Scholar and Professor of Classical Languages and James A. Barham, Dr. of History and Philosophy of Science. Thank you for all of your efforts in raising me. I am humbly appreciative.

Table of Contents

List of Tables

List of Figures

List of Abbreviations and Nomenclature

c^E	Stiffness at Constant Electric Field	$[Pa]$
d	Piezoelectric Constant	$[\frac{pC}{N}]$
D	Electric Displacement Field	$[\frac{C}{m^2}]$
EMT	Eletromagnetic Transformer	
H	Electric Enthalpy	$[\frac{J}{m^3}]$
J	Bessel Function	
L	Lagrangian	$[J]$
MEMS	Micro Electro Mechanical Systems	
PT	Piezoelectric Transformer	
PZT	Lead Zirconate Titanate	
Q	Mechanical Quality Factor	
Q_{Area}	Electrical Surface Charge Per Unit Area	$[\frac{C}{m^2}]$
Q_z	Electrical Charge	$[C]$
r	Cylindrical Radial Coordinate	$[m]$
S	Strain	$[\frac{m}{m}]$
S_r, S_θ	Radial and Angular Strain	$[\frac{m}{m}]$
s^E_{xx}	Compliance at Constant Electric Field	$[\frac{1}{Pa}]$
T	Stress	$[Pa]$
t	Disc Thickness	$[m]$
u_r	Radial Deflection	$[m]$
V	Electrical Potential Difference	$[V]$
W	Virtual Work (Surface Tractions and Charges)	$[\frac{J}{m^2}]$
z	Cylindrical z-Coordinate	$[m]$
$\epsilon^{T,S}$	Permittivity at Constant Stress/Strain	$[\frac{F}{m}]$
θ	Cylindrical Angular Coordinate	$[m]$
ν	Poisson's Ratio	
ρ	Density	$[\frac{kg}{m^3}]$
τ	Shear Stress	$[Pa]$
ω	Frequency	$[\frac{rad}{s}]$
$\ddot{a}$	Dots Represent Temporal Derivatives	
$a_{,tt}$	Commas Represent Spatial Derivatives	

Chapter 1: Introduction

1.1 Electrical Voltage Transformation

Voltage transformation, the process of increasing or decreasing (known as boosting or bucking, respectively) electrical potential energy per unit charge, measured in units of Volts (V), is fundamentally required in many electronic systems because of a mismatch between supplied voltage available to a system and its voltage demands. For example, in the case of an electrochemical battery supply, voltages are determined by the difference in electrical potential between the positive and negative electrodes, relative to an electrolyte (e.g. 3V of open-circuit voltage can be obtained in one battery cell utilizing a lithium iron phosphate cathode and carbon anode [23]). If an electronic system using such a 3V battery cell needs other voltages, such as 1.5V to run a microprocessor, and 9V to run a motor, it's often more efficient to transform the voltage given by the 3V battery into 1.5V and 9V, rather than adding extra batteries. Electronic systems over the last 25+ years have strived to achieve the lowest power consumption (e.g. less than 1.5V supply voltage [24]), in order to maximize computation cycles per unit of energy consumed. Therefore, efficient voltage transformers that can bridge the gap between these lower requirements and higher ones needed by, e.g. LCD backlighting requirements [25] in modern laptops

have become more important in the late 20th and early 21st centuries.

Electromagnetic voltage transformers (EMTs) have been in use since 1885 [26, 27], and have ranged in size from large commercial power [28] to very small microelectronic designs [19]. Since the 1950s [29] a competing technology, the piezoelectric voltage transformer (PT) has been in development. In contrast to EMTs, which convert electrical energy to magnetic energy and back to electrical, PTs convert electrical energy to mechanical energy (in the form of vibrations) and back to electrical using materials with piezoelectric properties (see subsection 1.4.1). In addition to voltage transformation, EMTs and PTs can perform other useful functions discussed in section 1.4.2.

1.2 Research Opportunities: Microfabricated Voltage Transformers

As of this writing, the landscape of voltage transformation devices spans from macro devices at the centimeter scale that have been commercialized in consumer laptop liquid crystal display electronics and can be bought for tens of dollars (Micromechatronics, Inc.), to research applications at the micrometer scale [30]. Generally speaking, macro piezoelectric transformer devices are more than one millimeter in thickness, and are produced using techniques such as sintering, while micro scale devices can be as thin as several micrometers, and are produced using microfabrication techniques such as sol-gel [31]. Electromagnetic devices typically require winding coils of wire, and can also be challenging to produce at smaller size scales, but work is being done in this area [32] as well. Interest in these devices at sub-cm

scales is due to increasing interest in the area of micro-robotics and micro power systems in general [21, 32, 33].

1.2.1 Addressing Research Opportunities

The present work will address research opportunities in the area of microfabricated voltage transformers by considering bulk piezoelectric devices. As outlined in section 1.3, piezoelectric devices have inherent advantages over electromagnetic devices including higher energy density for similar power densities, and as outlined in section 1.4 there is currently a gap in the research between thin-film micro scale devices and macro scale solutions. Modeling and analysis will be used to drive design decisions for the devices in question, and prototypes will be built and tested to evaluate their performance and for comparison to the theoretical predictions. The end goal is to microfabricate piezoelectric transformers smaller than prior work, while maximizing voltage gain.

1.3 Comparison of PTs and EMTs; Power, Energy Density and Efficiency

EMTs are well known to most electronics engineers, due to being covered in undergraduate and graduate engineering curricula, and have been in widespread use for over a century. PTs, on the other hand, being newer technology, are not as widely known and understood. Their basic properties and constitutive models have been discussed [34, 35], but it may not be clear what applications call for PTs vs

EMTs. The present work compares PTs and EMTs in terms of energy density, power density, efficiency and device volume, in order to attempt to draw some conclusions about the relative merits of each.

Energy and power density are important engineering metrics that, generally, indicate how much energy a device can store (per its volume or mass) at a given time, and how quickly the device can deliver that energy to its load (also per its volume or mass). Because EMTs and PTs temporarily store energy in electromagnetic fields and mechanical vibrations (phonons), respectively, while operating, they can be considered energy storage devices. Their primary goal is not to store the energy for long periods of time, like batteries and capacitors, but to convert energy and transfer it to a load quickly and efficiently. When designing power systems from the MEMS (micro) scale [36] all the way up to large commercial power scales [37], designers repeatedly stress the need for high energy and power density, not just in their energy storage elements, but in the entire system, of which the EMT or PT is one important component.

Efficiency and device manufacturability are also key metrics when comparing microsystem components. As shown in figure 1.3, both EMT and PT devices are capable of high efficiency operation, but overall PTs in the literature operate at higher efficiencies than EMTs. Manufacturability/microfabrication of devices has also been addressed in small-scale EMT and PT devices [21, 32, 38], with PT challenges including piezoelectric material properties at micron thicknesses, and EMT challenges including winding miniature bobbins with wire coils.

1.3.1 Maximum Theoretical Energy Density

Theoretical maximum energy densities of EMTs and PTs reported in the literature are summarized in table 1.1. For completeness, Electrodynamic Transformers (ETs), a third competing technology based on moving mechanical structures, which theoretically appears promising but has not reported successful prototypes on the level of PTs and EMTs as of this writing, are also included. This list of values does not appear to provide conclusive evidence that one technology is superior in terms of energy density to others, as authors differ widely on their estimates, over several orders of magnitude. For comparison, the highest energy density devices that turned up in my literature search were less than 0.002J cm^{-3} [1, 8].

Table 1.1: Theoretical Maximum Energy Density of EMTs, ETs and PTs

Technology	Energy Density [J cm^{-3}]	Notes	Ref
ET	2 - 1,000	ET at 50 Hz	[39, 40]
PT	1	"Maximum Energy Density in PZT"	[39]
EMT	0.1	"Maximum Magnetic Energy Density"	[39]
PT	0.035	"Piezoelectric maximum energy density (PZT 5H)"	[41]
EMT	0.025	"Electromagnetic maximum energy density (0.25T)"	[41]
PT	0.004	"For a specific PZT 5H sample considered"	[42]

1.3.2 Power and Energy Density Charts

Figures 1.1, 1.2 and 1.3 are based on the PT and EMT literature, and include prototype devices only, not theoretical or predicted results from modeling. They serve to give an overview of the current transformer landscape, and offer a way to compare different technologies. The Ragone style of chart [43], which was popularized in the field of energy storage, is utilized in figure 1.1, and directly compares devices on energy and power density metrics. These results are from different researchers often working towards disparate goals, and were not all designed to maximize their power and energy density, so these results are not an absolute measure of the relative worth of different prototypes. For example, the present work considers only 3V-6V input voltages, because this is a typical range for small scale systems, but if higher input voltages were used, higher output power density would also result. Power and energy density were calculated from output power of the devices, divided by their volume or density, and using the operating frequency reported. In thin film devices where thickness dimensions weren't reported explicitly, a typical 4 inch silicon wafer thickness of 0.525mm was assumed. If piezoelectric or copper material densities weren't reported, 7800Kg m^{-3} and 8960Kg m^{-3}, respectively, were assumed. The numbers in the charts correspond to the literature references of the same number in the bibliography.

Based on Figure 1.1, PTs are advantageous over EMTs when considering device energy density. Some EMTs based on thin metal deposition show high power density (due to their small thickness), but are also not scalable across different orders

of size, as bulk PT devices are.

1.4 Prior Work

PT technology development over the past 60 years has focused on bulk materials, with most fabricated macro scale devices' volumes on the order of 0.1-1.0cm^3. Within the last decade, researchers have also reported thin-film PZT technology based on chemical deposition techniques [31, 38, 45], leading to devices on the order of .0003cm^3, several orders of magnitude smaller than bulk PT devices. The present work is situated in between these two size extremes, with the highest performing devices in the present work on the order of .002cm^3, and strives to strike a balance between device size and fabrication complexity.

1.4.1 Materials

The Greek word piezein can be defined as "press, squeeze, or crush" (related to pressure), and piezoelectric materials have coupled electrical and mechanical properties, meaning that exciting them with electrical energy can motivate them to mechanically deform / become stressed / produce a force, and conversely, mechanically deforming / stressing them will cause them to produce electrical potential energy, which can be used to motivate an electric current [46].

"Bulk" is typically used to denote materials made with macro scale processing techniques such as casting, sintering, molding, etc., often involving moles of atoms interacting at a given time to create the material, and whose dimensions are typ-

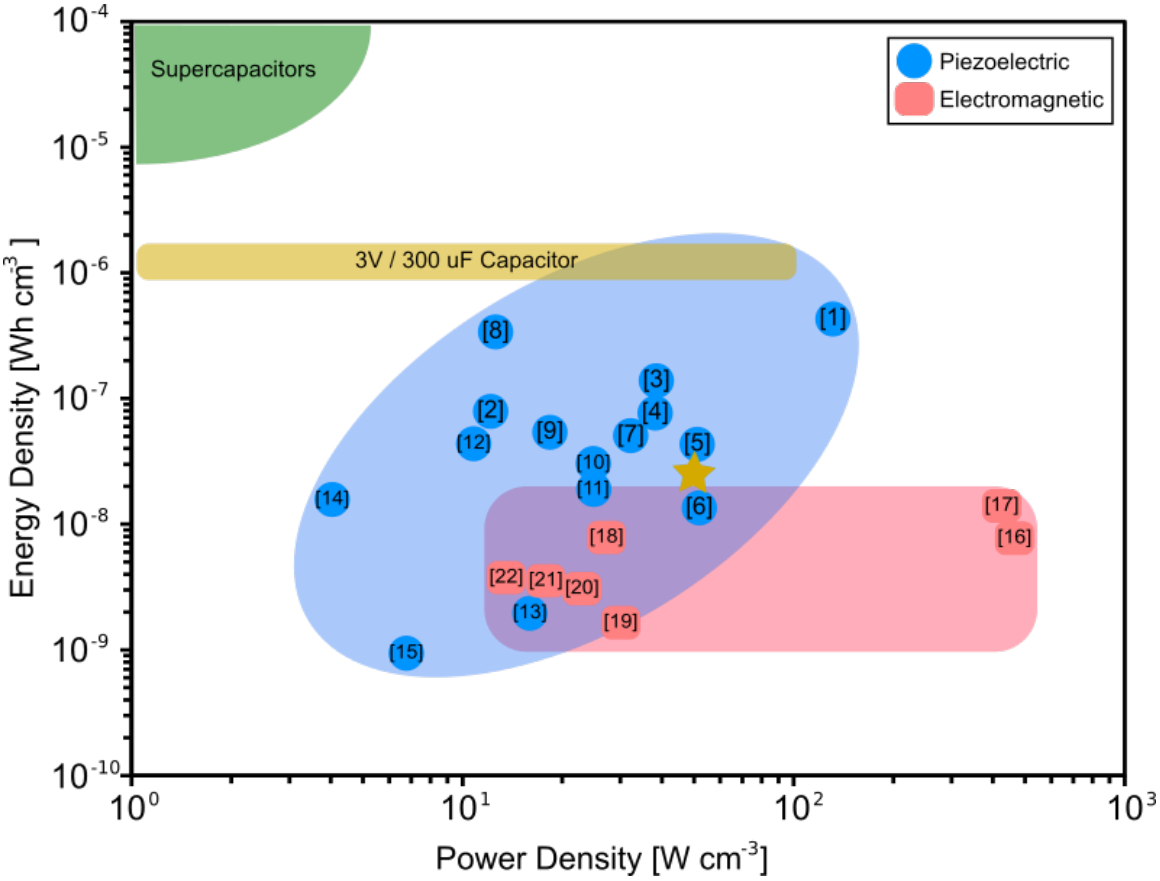

Figure 1.1: Volume Ragone Chart: PT and EMT devices reported in the literature; star represents the present work (4mm diameter disc PT, area ratio = 1, 1MΩ load). For a given power density, PT devices trend towards higher energy density, compared to EMTs, and therefore may be more beneficial to microsystem designers. Supercapacitor and electrolytic capacitor device ranges are from [44] and identification numbers on the plots correspond to reference numbers in the bibliography.

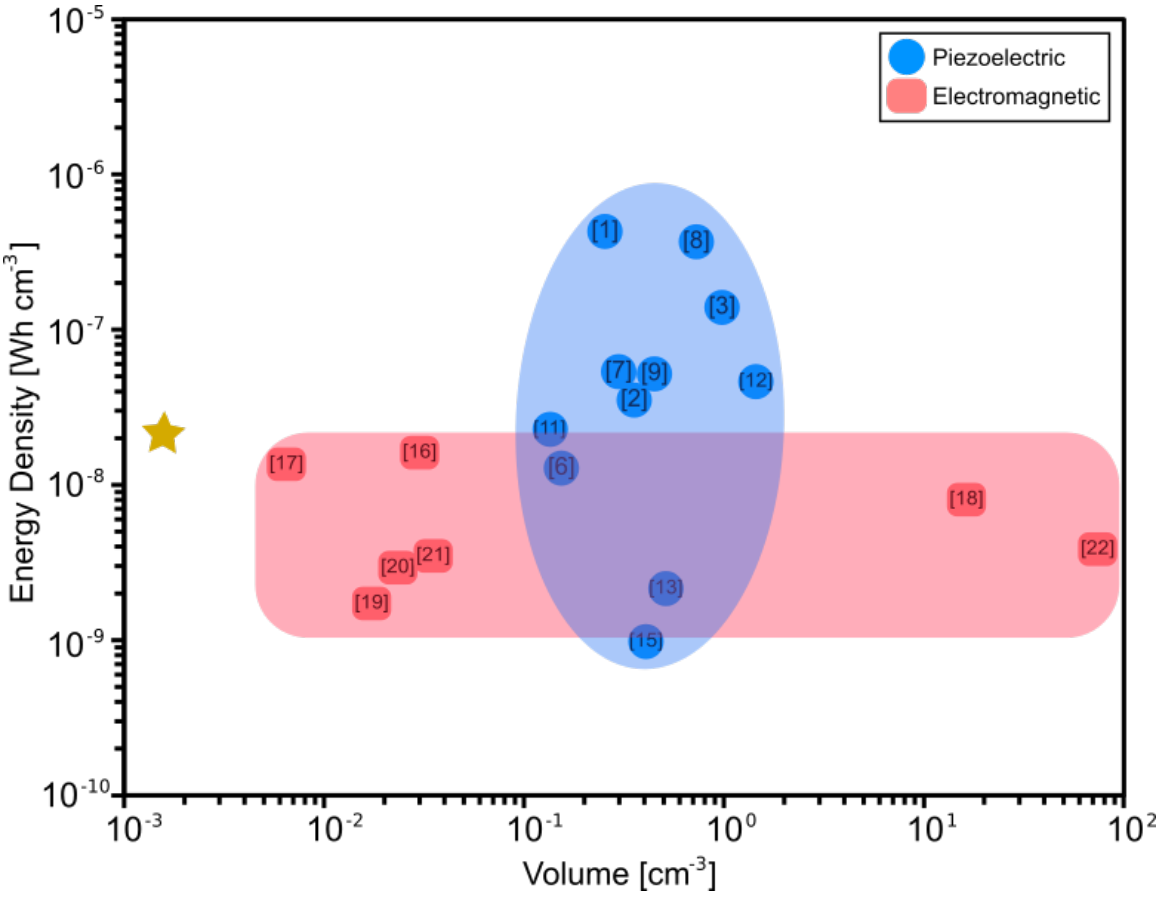

Figure 1.2: Volume vs. energy density of PT and EMT devices reported in the literature; star represents the present work (4mm diameter disc PT, area ratio = 1, 1MΩ load). The present work is roughly one order smaller by volume than the smallest reported EMT and PT literature (excluding thin-film PT devices, which have not reported output power as of this writing), with equivalent energy density to EMTs, and lower energy density than larger-scale PTs. This demonstrates that despite the small volume of the present work, its energy density is equal to or better than other, larger, devices in the literature, while not matching the highest performing devices reported.

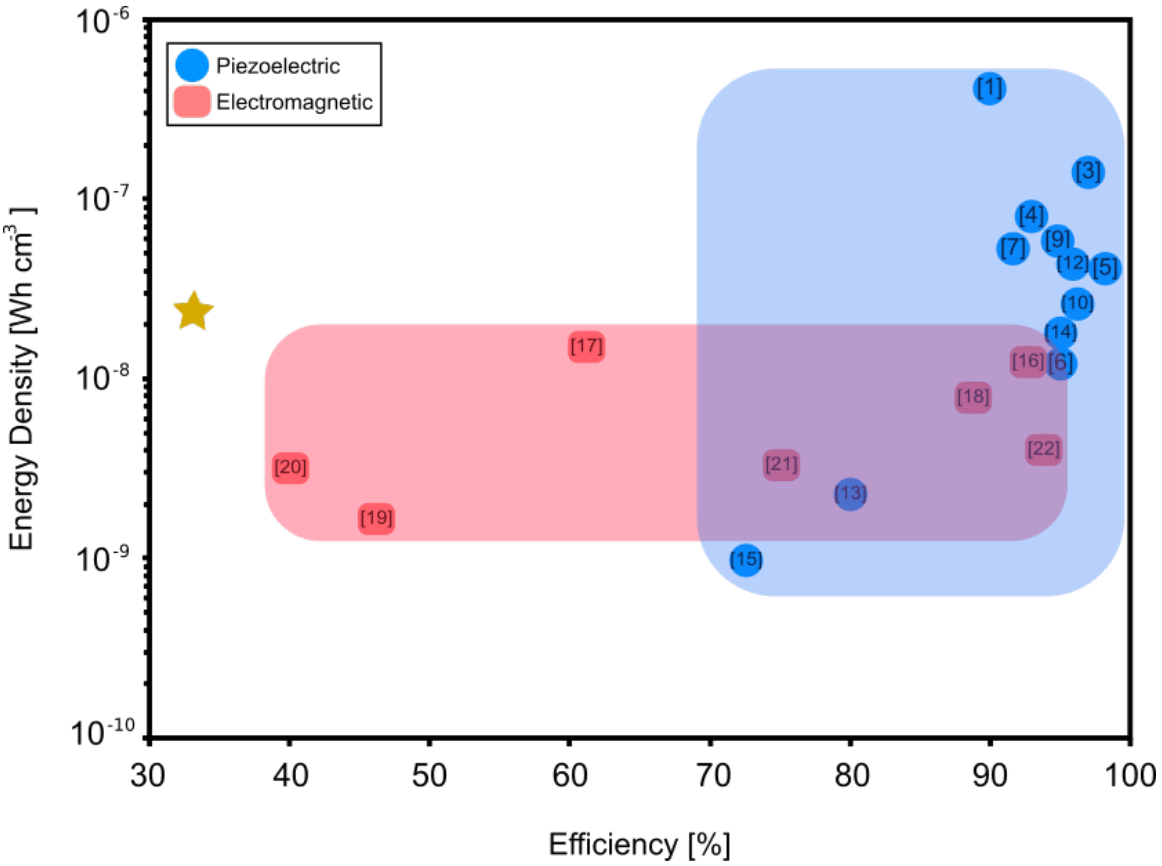

Figure 1.3: Energy density vs. efficiency of PT and EMT devices reported in the literature; star represents the present work (4mm diameter radius disc PT, area ratio = 1, 1MΩ load). Both PT and EMT devices are capable of achieving over 90% efficiency, while on average PT devices show higher efficiency than EMT. The present work, which is several orders smaller by volume than the bulk PT literature, is also less efficient than larger devices. Potential solutions to raise the efficiency of the present devices are addressed in Chapter 5.

ically measured in millimeters, centimeters and meters. Bulk devices are typically larger-scale, as opposed to thin-film materials/devices, which are typically created using chemical deposition techniques on top of a thicker structural base substrate, with the active material thickness usually measured in angstroms, nanometers or micrometers.

The mechanics of piezoelectric materials is based on the linear theory of piezoelectricity [46], which gives the equations governing the "direct" (deformation to electrical energy) and "reverse" (electrical energy to mechanical deformation) piezoelectric effects. All piezoelectric materials have both direct and reverse properties, collectively known as the piezoelectric effect.

Materials with piezoelectric properties are both naturally occurring (e.g. Quartz) and man-made (e.g. Lead Zirconate Titanate - PZT). Table 1.2 shows the relative place piezoelectric materials occupy among known classes of crystals (Section 3.5 of Ref. [46]). Of note, in addition to the piezoelectric effect described above, some piezoelectric materials also have pyroelectric (sensitivity to heat) and ferroelectric (hysteretic effects during poling) properties.

The piezoelectric effect can be amplified in a given subset of piezoelectric materials known as ferroelectrics through a process known as electrical poling. This process uses a large electric field to align a material's atomic dipoles in a given direction, causing them to electrically align, as opposed to their pre-poling, randomly oriented orientation. This process is analogous to magnetic poling of a weakly magnetic material (with randomly oriented magnetic dipoles), to line up its magnetic atomic dipoles and thus produce strong north and south poles on opposite faces of

the magnet.

In the last 50 years the most popular materials for many piezoelectric applications have been PZT variants, due to their relatively high electromechanical coupling and piezoelectric properties [13, 47–55]. More recently, other materials have been investigated, due in part to environmental regulations such as the European Union Restriction of Hazardous Substances Directive (RoHS) adopted into EU law in 2003 [11]. General guidelines for material investigation have been suggested [56], along with specific investigations into the following alternative materials, some of which are reporting performance approaching or exceeding that of PZT [4, 7, 11]:

- Sodium Niobate (NN) [7]
- Sodium Potassium Niobate (NKN) [11, 57–59]
- Barium Titanate (BT) [60, 61]
- Lead Magnesium Niobate-Lead Titanate (PMN-PT) [4, 62]
- Multiferroic Review Papers [50, 63]
- General Review Papers [51, 64]

Table 1.2: Classes of Crystals

<table>
<tr><td colspan="4">32 Crystal Classes</td></tr>
<tr><td colspan="3">20 Piezoelectric Classes</td><td>12 Non-piezoelectric</td></tr>
<tr><td colspan="2">10 Pyroelectric Classes</td><td>10 Non-pyroelectric</td><td></td></tr>
<tr><td>Ferroelectric</td><td>Non-ferroelectric</td><td></td><td></td></tr>
</table>

Table 1.3 summarizes the material properties of the PZT used in this study, sourced from Piezo Systems, Inc. Because the full material property matrices were not available from the manufacturer, for modeling purposes PZT-5 properties from the literature [65] were used (see table 1.4).

Table 1.3: Material Properties of PZT-5A Sourced from Piezo Systems INC: Relative Permittivity ϵ_{rel}, Piezoelectric Constants d; Density ρ; Mechanical Quality Factor Q; Stiffness c

Property	Value	Units
$\epsilon^{T}_{rel,33}$	1800	1
d_{33}	390e-12	$\frac{m}{V}$ or $\frac{C}{N}$
d_{31}	-190e-12	$\frac{m}{V}$ or $\frac{C}{N}$
ρ	7800	$\frac{Kg}{m^3}$
Q	80	1
c_{33}	5.2e10	Pa
c_{11}	6.6e10	Pa

1.4.2 Applications

There are various applications of PTs reported in the literature, some of which will be reviewed here. Vasic et al. used PTs to drive transistor gates, in order to limit parasitic coupling and increase reliability [15, 66]. Reliability of electrical systems in general can be increased through the use of PTs to provide galvanic isolation between components [66, 67]. DCDC [60] and ACDC [68] conversion and voltage rectification [68] can be accomplished through the use of PTs; in the case of DC operation, both inverting and/or rectification circuits are needed to convert between DC and AC signals, which would slightly lower overall system efficiency. PTs can be connected in parallel [69] and in series [70] in order to change their characteristics and increase current/voltage/power output. Geometry has been considered involving a single device with multiple disparate output sections [6], and converters have been used on large scale wind turbine systems [37].

In addition, research is ongoing in the area of miniaturized robotics, and there is an associated need for miniaturized power systems [21, 32, 33]. This is one area where small, energy dense PTs may be useful.

Different PT topologies have been reported in the literature, including thin discs [71, 72], free-free beams [38], Rosen bars [73, 74] and rings [75]. Each topology has benefits and negative aspects, but overall Rosen bar-type devices have shown the highest gain experimentally and have been commercialized on the macro scale more than any other topology.

In this work thin discs (Chapter 3) and free-free beams (Chapter 4) based on 0.127mm thick PZT were considered due to their fabrication and performance advantages. Uniform topologies (one single piece of material) were considered here because of fabrication advantages over Rosen bar type transformers, which do not lend themselves to microfabrication. The present work consists of one bulk material layer poled in a single direction, as opposed to Rosen bar transformers which are composed of two different material sections, mechanically attached to one another and poled in different directions.

1.4.3 Related Technology: MEMS Mechanical Filters and Resonators

Mechanical filters operate through the principle of electrical-mechanical transduction (analogous to piezoelectric transduction in the present work), typically transforming electrical input signals into mechanical movement, performing filtering mechanically, and transforming the mechanical filtered signal back into an electrical

output [76, 77]. Filters and resonators were some of the first devices investigated in the MEMS field, starting in the 1980s, because of their ability to offer temperature-stable, high-quality filtering and reference frequencies for communication applications.

Devices in the present work are not intended to provide signal filtering or frequency reference as their primary design objective, but nonetheless have common features with previously developed resonating MEMS devices, which will be reviewed here. Common features include vibration frequency selection (high gain voltage output at resonance, combined with low gain off-resonance), and a desire to maximize quality factor and limit losses during operation. The main difference between the present PT devices and previous filter/resonator devices is the scale, with present devices fabricated using bulk-scale material, which has the advantage of higher piezoelectric coefficients, in some cases twice the values seen in thin-film materials [78]. Present devices are also more economical to fabricate, due to the reduced processing times associated with bulk material fabrication schemes, compared to thin-film deposition methods.

The small physical dimensions of MEMS filters and resonators enable smaller footprints than competing technologies, sub microsecond response times, and high-frequency operation, which leads to usable levels of output power for certain devices, despite the small size [77–79]. Typical device dimensions are as follows: device layer thickness of several micrometers; gap between device layer and ground plane of several micrometers; length and width from single to tens of micrometers [76]. Typical DC offset voltages required for operation can range from tens to hundreds

of volts [76]. Vibrating MEMS devices have been reported in a number of different topologies, including [80]: clamped-clamped and free-free beam, centrally-supported disc (wine-glass) and contour-mode (in-plane resonant) disc, and supported ring (see Table 1.5). Comparisons were also made between one-port and two-port devices, with two-port designs (such as the present PT devices) having the advantage of supporting differential signals and allowing input and output impedance tuning through the input and output capacitances [77]. All of these topologies are differentiated by tradeoffs between fabrication complexity and device performance, with beams being relatively straightforward to fabricate, and centrally-supported discs showing some of the highest quality factors at high frequency.

It is important to mechanically support MEMS resonant devices in an efficient manner during operation, in order to avoid energy loss and achieve optimal performance. For example, mechanical clamping/tethering losses can lead to a reduced device quality factor as operating frequency increases [76]. These inefficiencies can be minimized in a number of ways. When feasible, utilizing a single anchor can increases the quality factor/efficiency of a resonator, when compared to multiple anchors, but anchor size can also affect resonant frequencies of devices [81]. In several studies, two-anchor solutions were found to be preferable to four-anchor due to the four-anchor tethering scheme limiting device deflection [82] and reducing quality factor [77]. Another approach is to base the design off of the wavelength of the resonant frequency of interest, for example to fabricate tethers that are one quarter of a wavelength in length, in order to reflect vibration energy and not transmit it to the surrounding structure [80, 81]. This approach is not universally accepted,

however, and some authors see it as an insufficient solution [83], and are in favor of other means, e.g. acoustic reflectors.

In the present work both beam and disc PT topologies are investigated, and, as in the filter literature, beam topologies are more straightforward to fabricate. Ring geometries were not considered due to the lack of surface area for locating input and output electrodes needed for PT operation. The MEMS filters with the highest quality factors were discs supported at their central node location (wine-glass); however, this tethering scheme was not possible with the present PT fabrication process (discussed in Chapter 2). The present disc PTs, tethered at their periphery, had lower quality factors than free-free beam PTs, tethered at their nodal locations. If it had been possible to tether disc PTs at their central nodal location, given the present fabrication process, this would likely have constrained device movement less during operation, leading to improved performance. Compared to the resonant MEMS literature, the present work also has the following significant differences: the present devices are larger in scale (by at least one order of magnitude); operate in air (non-hermetic environment); vibrate in-plane instead of in a transverse direction (in some cases); operate at roughly 5 Volts AC input without DC offset, instead of 10s to 100s of Volts DC offset; and have tethers defined from active rather than passive material. These differences result in different design decisions in the present PT work, than might be expected in the MEMS resonant literature. For example, the mass of a 500nm layer of deposited Al on 127μm thick PZT in the present work has negligible impact on device resonance; however, such added mass would noticeably affect the resonance frequency of single-micron thickness MEMS resonators,

where this mass loading would be significant compared to the device's initial mass. The larger size, operation in air, and lack of large DC offset voltages of the present PT devices, compared to the filter literature, led to the significant differences in quality factor observed, with present devices orders of magnitude lower than the highest reported literature values. Tethering approaches used in the present work, and further design details are covered in detail in Chapters 3 and 4.

1.5 Modeling Tools

In order to facilitate the design of complex devices such as those in the present work, computer and analytical tools are often used to model the system, with the goal of more fully understanding how it functions and aiding in design decisions. Computer finite element analysis code and analytical mathematical modeling were used here. Please see appendix A for information on how to download copies of the code, if interested in learning more.

1.5.1 Finite Element Analysis

PT behavior is difficult to predict analytically for arbitrary geometries and electrode configurations, and the finite element method of analysis (a.k.a. FEM or FEA) has been employed extensively in modeling piezoelectric systems [73, 74, 84–87]. This effort made use of the commercial FEA code Comsol Multiphysics 5.1 (Comsol, Inc 2017) to predict PT behavior and provide a comparison with the analytical theory and experimental results. This package provides the ability

to model piezoelectric material, which encompasses mechanics and electrostatics, along with acoustic and electrical circuit physics (the latter is useful for varying load resistance at PT output) in one integrated platform. Additionally, internal damping (inefficiencies) were included. The included piezoelectric material model has options for adding mechanical damping, coupling loss, dielectric loss and conduction (time-harmonic) loss. Of note, the "isotropic loss factor" accessible through "coupling loss" is equal to the inverse of the device quality factor, as discussed in Chapter 3. Therefore the quality factor of a given material, reported by the manufacturer or obtained experimentally, can be directly integrated into a PT FEA model. In the present work good correlation has been found between predicted FEA results and experimental results when quality factors obtained experimentally were used in numeric models, for certain loading conditions. FEA models have the advantage of being able to subdivide device geometry into small fractions of a wavelength, solving constitutive equations at small length scales, and so can perform better than analytical models in certain cases.

1.5.2 Analytical Approaches

Analytical modeling of PTs is difficult because phonon wavelengths are on the order of the devices in question (see Table 1.6). Most analytical models in the literature simplify the system down to lumped parameters [88], and in order for this to be a valid approximation, the energy in question should have a wavelength at least 1.5 orders higher than the device in question (Ref. [89], pg. 69), so that

there is no significant phase difference in the energy wave as it passes across the device. Considering Table 1.6 (assumed speed of sound in PZT = 2,580m s^{-1} [90]), distributed electrical modeling, nonlinear structural mechanics modeling, and/or other modeling strategies such as those using energy methods (considered here) may be more appropriate for piezoelectric transformers than lumped parameter modeling.

The advantage of analytical modeling is that it affords the system designer more personal insight into the problem at hand. Rather than using a "black box" software package, where input and outputs are recorded, but the derived constitutive equations and method of problem solution are not known to the average user, an analytical approach allows full transparency. This increased transparency enables the system designer to more clearly identify the relationships between design variables. The system designer can use this knowledge to more efficiently design a device with the desired characteristics, and within design constraints.

Another factor to consider in piezoelectric material modeling is the appearance of system nonlineraities. Researchers have found while studying piezoelectric transformers that high output loads cause nonlinear behavior to become non-negligible [91]. Additionally, various researchers have reported that the behavior of piezoelectric transformers can exhibit nonlinearities such as multi-valuedness / voltage jumping, which stem from their nature as resonant devices [25, 92–96].

Table 1.4: PZT-5 Properties Used in Modeling: Piezoelectric Constants d; Compliance s; Relative Permittivity ϵ_{rel}; Poisson's Ratio ν

Property	Value	Units
d_{31}	-172	$\frac{pC}{N}$
d_{33}	374	$\frac{pC}{N}$
d_{24}, d_{15}	584	$\frac{pC}{N}$
s_{11}^E, s_{22}^E	$1.64e-11$	$\frac{1}{Pa}$
s_{12}^E	$-5.74e-12$	$\frac{1}{Pa}$
s_{13}^E, s_{23}^E	$-7.20e-12$	$\frac{1}{Pa}$
s_{33}^E	$1.88e-11$	$\frac{1}{Pa}$
s_{44}^E, s_{55}^E	$4.75e-11$	$\frac{1}{Pa}$
$s_{66}^E = \frac{1}{2}\left(s_{11}^E - s_{12}^E\right)$		$\frac{1}{Pa}$
$\epsilon_{rel,33}^T$	1700	1
ν	$-\frac{s_{12}^E}{s_{11}^E}$	1

Table 1.5: Previously Reported MEMS Filter and Resonator Devices [80]

Type	Description	Performance
Clamped-Clamped Beam	$2\mu m$ thick, $40\mu m$ long	Q=50 (air) at $10MHz$, Q=300 at $70MHz$
Free-Free Beam	$14\mu m$ long	Q=2,000 (air) at $90MHz$
Wine-Glass Disc	$53\mu m$ diameter	Q=8,000 (air) at $98MHz$
Contour-Mode Disc	$10\mu m$ diameter	Q=10,000 (air) at $1{,}500MHz$
Spoke-Supported Ring	$10\mu m$ wide; $122\mu m$ diameter	Q=10,000 (air) at $1{,}500MHz$

Table 1.6: Ratio of Wavelength to Output Dimension Across Devices of Different Scale (assumed speed of sound in PZT = 2,580 m s^{-1})

Output Dimension $[m]$	Frequency $[Hz]$	Wavelength $[m]$	Wavelength / Output Dim.	Ref.
1E-02	1.25E+05	2.06E-02	2.06	[88]
2E-03	5.50E+05	4.69E-03	2.35	This Work
2E-04	1.90E+07	1.36E-04	0.68	[38]

Chapter 2: Microfabrication and Testing Methodology

2.1 Microfabrication

In order to microfabricate piezoelectric transformers quickly and accurately at the micrometer scale, a combination of techniques including photolithography [97] and micropowder blasting [98] were employed in the present work. Micropowder blasting, which is used commercially to engrave glass, is not widely used in microtechnology, and employs dry-film photolithographic masking combined with mechanical ablation of a sample with μm-scale hard particles. It is beneficial due to being faster/cheaper than etching methods such as deep reactive ion etching, while being more accurate than other fast methods such as wet etching. This etching process addresses a need for fast bulk piezoelectric material etching methods reported previously [78]. A benchtop microabrasive blasting workstation (MicroBlaster, Comco, Inc.) and $25\mu m$ alumina particles were utilized.

In the present work aluminum (Al) evaporation and wet etching for electrode patterning, and micropowder blasting for selective PZT etching, were combined in a two photomask process to fabricate bulk piezoelectric transformers from a 7.24cm square, 0.127mm thick PZT sheet (Piezo Systems: PZT-5A sheets (PSI5A4E)). In order to provide a robust substrate for handling during processing, the PZT was

temporarily bonded to a 10cm diameter silicon wafer using a sacrificial layer of adhesive wax (Crystalbond 509). Bonding was performed by mounting the PZT sheet manually on melted wax at 90°C. The PZT is manufactured with nickel metal layers on top and bottom sides, and the top device side nickel was removed using a 1.5min wet etch (nickel etchant TFB, Transene Inc), to allow for a better controlled device layer metal deposition. Afterwards, the transformer input and output electrodes were patterned by the following process: 500nm Al electron beam evaporation (NexDep Ebeam Evaporator, Angstrom Engineering); 1.5μm thick spin coated positive imaging resist (Shipley Microposit s1813, Dow Electronic Materials); UV exposure (with electrode pattern mask) (EVG 620, EV Group); 1min resist development (Shipley MicroDev, Dow Electronic Materials); Al wet etch for 30s at 65°C (Al Etch Type D, Transene Inc). Before micropowder blasting, a 100μm thick dry film photoresist (RapidMASK High Tack) was laminated on the PZT sample as an etch mask in a commercial laminator, followed by UV exposure of the second (powderblasting area) mask. The micropowder blasting parameters used were: nozzle pressure of 552kPa; 457μm nozzle diameter; 4cm standoff distance from sample.

After microfabrication and testing of the devices in this work, and the failure of the smallest devices to achieve resonance, questions arose as to whether there were any potential issues with the above process. Another student in our research group, Prakruthi Hareesh, determined that there was an issue with the above process causing the outer 300μm of each device to become damaged and lose piezoelectric coupling properties, and as of this writing is developing an improved microfabrication process to address this issue. In the present work, the lower limit of the stated

fabrication process has been found, and simulation models were modified to take into consideration a $300\mu m$ zone of material without piezoelectric coupling at the periphery of each device.

2.2 Testing

Device testing (Figure 2.1) consisted of the following process. A sinusoidal voltage input between 3V-6V was created by a signal generator (Hewlett Packard 33120A), corresponding to a typical voltage range produced by 1-2 lithium ion battery cells, a common component in micro scale systems. This input voltage was fed through a high output impedance op-amp buffer (LM6172IN, Texas Instruments), a 50Ω resistor (R_1) and into the input of the transformer. The output of the transformer was fed through a 100Ω resistor (R_2) and to the variable output load resistor. The small 50Ω & 100Ω resistors were added to the circuit to enable current measurement without the use of an expensive current probe. Voltages V_1 through V_4 were recorded with an oscilloscope, through another op-amp buffer to minimize the effect of measurement on the circuit performance (except where noted), and current was calculated via Ohm's Law, which enabled calculation of power and efficiency. The back side ground plane of the PT was electrically connected to the test setup common ground.

Statistics were gathered by repeated (greater than or equal to 3) measurements of a given fabricated device; there were not enough devices fabricated to provide at least 3 different prototypes for each area ratio/radius combination. Number

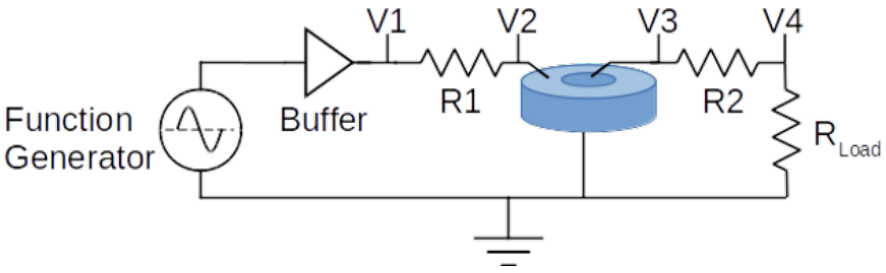

Figure 2.1: PT experimental testing schematic

of measurements was marked $n = x$, and error bars shown are to one standard deviation. In cases where standard deviations were less than two percent of mean values, error bars were omitted (e.g. many gain results were highly consistent across repeated measurements).

Chapter 3: Circular Radial Mode PTs

3.1 Introduction

The first microfabricated topologies were thin circular discs, with concentric "ring-dot" electrode configurations. The ring-dot electrodes were on the top face of the devices, and a conformal electrode covered the entire bottom of the devices. Voltage inputs and outputs were relative to the bottom electrode plane of the devices, with the input electric field actuating the device in the thickness direction via the outer annulus electrode, transmitting lateral mechanical stress to the central portion of the device, which in turn generated a second and different electrical potential at the central output electrode (also relative to the bottom ground plane). This electrode arrangement was chosen due to previous studies showing that this structure, and the radial "breathing" or "kp" mode it motivates, was the most efficient in a circular thin-disc topology [71, 99]. Out-of-plane bending modes necessarily have to displace more air on the top surface of the device, as opposed to radial modes which only displace smaller amounts at their periphery. This radial mode behavior should be beneficial as devices are scaled down and air damping potentially becomes more problematic. Rectangular thin discs vibrating in-plane were not considered, due to predicted lower efficiency caused by asymmetric phonon reflections at their

edges, which create additional non-fundamental vibrations in the device [84].

When designing electrodes, there are three variables to consider: input area, output area, and gap between input and output sections. All three of these variables combine to define the area ratio (AR) of the device, defined as the area of the input annulus electrode divided by the area of the output inner circular electrode. By optimizing a device's area ratio for a given desired mode and output loading condition, maximum performance can be achieved for a given device diameter.

Previous literature in circular disc type bulk PTs reported the effect of different device topologies on the basis of electrode area ratio. On this basis, three different groups reported that the maximum voltage gain of their highest output power device was realized for AR values less than 20. All reported devices had efficiencies greater than 80 percent. This and other pertinent information is summarized in table 3.1. Of note, the bulk PT literature is several orders larger in volume than the present work.

The devices reported here have electrode area ratios between 1 and 4, which result in a range of varying performance at different electrical loads, for the same device dimensions. Consistent with the previous work, the area ratios fell below the AR=20 threshold indicated for maximum voltage gain.

The devices in this work are tethered, to allow them to expand radially, while mechanically supporting them to allow for integration into an electro-mechanical system. Tethering is not addressed in the majority of the bulk circular PT literature, but tethers are commonly found in micro-devices, and two common designs are serpentine [100, 101] and folded-beam [30, 102]. Folded beam designs were selected

due to achieving comparatively higher out-of-plane stiffness, in order to support the transformer in its desired plane of movement, while being compliant enough in said plane to allow the device to vibrate. Serpentine springs would provide less support to the resonant devices during operation, and $\lambda/4$ matching designs used in some mechanical resonant filters were not considered due to several factors. First, the monolithic tethers in this application were made from active material, making them more difficult to model as static boundary conditions. Second, at a 550kHz primary resonance for a 4mm diameter device, $\lambda/4 = 1.2$mm, which increases the footprint of the device and its standoff from the substrate compared to the as-manufactured folded beam tethers, and would not allow for further future miniaturization of the tethers.

Table 3.1: Literature Review of Circular Topology Bulk PTs

Volume $[cm^3]$	Area Ratio $[Input/Output]$	Voltage Gain $[Vout/Vin]$	Output Power [mW]	Ref.
2.6	0.09	2.0	50	[72]
0.4	3.00	1.0	12,000	[3]
0.4	6.50	40.0	8,000	[9]
0.0016	1.00	2.5	80	This Work

3.2 Analytical Piezoelectric Disc Modeling Review

Dynamic analysis of disc PTs is built upon an understanding of the equations of motion of a piezoelectric disc (Fig. 3.1), derived using structural mechanics and piezoelectric principles which will be reviewed here.

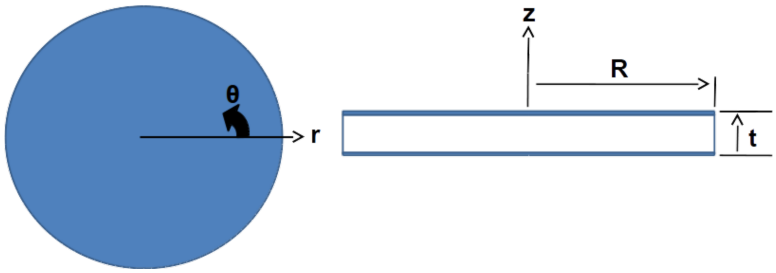

Figure 3.1: Schematic of Piezoelectric Disc, Covered on Both Faces by Conformal Electrodes, R is the Radius and t the Thickness

From Ugural and Fenster [103], section 3.3, the general thin plate plane stress assumption is as follows:

$$T_z = \tau_{xz} = \tau_{yz} = 0 \tag{3.1}$$

From Ugural and Fenster [103], section 3.6, the basic stress and strain relations in polar coordinates come from a force balance, with the assumption that shear terms are zero during radial expansion modes:

Equation of Equilibrium:

$$T_{r,r} + \left(\frac{T_r - T_\theta}{r}\right) + \rho\omega^2 u_r = 0 \tag{3.2}$$

Radial and Tangential Strain:

$$\begin{aligned} S_r &= u_{r,r} \\ S_\theta &= \frac{u_r}{r} \end{aligned} \tag{3.3}$$

Derivation of the constitutive linear piezoelectric equations was documented by Tiersten's book on plate vibrations [104], and later published in the IEEE Standard on Piezoelectricity [46]. Because of electromechanical coupling in piezoelectric

materials, the traditional mechanics and electrical terms of potential energy and electrical energy are replaced by one term encompassing both: the electric enthalpy H. H is a measure of the energy of the piezoelectric medium, and is defined as follows:

$$H = \frac{1}{2}c^E_{ijkl}S_{ij}S_{kl} - e_{ijk}E_iS_{jk} - \frac{1}{2}\epsilon^S_{ij}E_iE_j \tag{3.4}$$

The following relation (from the IEEE Standard) can be used to make a substitution into Eqn. 3.4, and is useful because d constants are more readily available from manufacturers than e constants.

$$e_{ip} = d_{iq}c^E_{qp} \tag{3.5}$$

Using the electric enthalpy H, Tiersten derives the linear piezoelectric constitutive equations in Cartesian form (Eqn. 3.6). Meitzler, another architect of the IEEE Standard, started with the standard linear piezoelectric relations in Cartesian coordinates and converted them to cylindrical coordinates, with the assumption that tangential deflections are zero for a thin disc with electrodes covering both faces (i.e. the disc motion is purely radial) [105]:

Cartesian Form:

$$\begin{aligned} T_i &= c^E_{ij}\left(S_j - d_{kl}E_k\right) \\ D_i &= d_{ij}T_j + \epsilon^S_{ik}E_k \end{aligned} \tag{3.6}$$

Cylindrical Form:

$$T_r = \frac{1}{s_{11}^E(1-\nu^2)}(S_r + \nu S_\theta) - \frac{d_{31}}{s_{11}^E(1-\nu)}E_z$$
$$T_\theta = \frac{1}{s_{11}^E(1-\nu^2)}(\nu S_r + S_\theta) - \frac{d_{31}}{s_{11}^E(1-\nu)}E_z \tag{3.7}$$
$$D_z = d_{31}(T_r + T_\theta) + \epsilon_{33}^T E_z$$

By substituting 3.7 into 3.2, the equation of motion for a bulk piezoelectric disc with electrodes on both sides is derived:

$$u_{r,rr} + \frac{u_{r,r}}{r} + (\lambda^2 - \frac{1}{r^2})u_r = 0 \tag{3.8}$$

with:

$$\lambda^2 = \omega^2 \rho s_{11}^E(1-\nu^2) \tag{3.9}$$

and assuming a traction-free boundary condition at the edge of the disc:

$$T_r\Big|_{r=R} = 0 \tag{3.10}$$

Equation 3.8 is in the form of Bessel's Differential Equation, and the solution therefore takes the form of a Bessel function, with its constant C_1 determined by boundary conditions:

$$u_r = C_1 J_1(\lambda r) \tag{3.11}$$

This type of approach has been used to describe piezoelectric disc dynamics in the literature [106, 107].

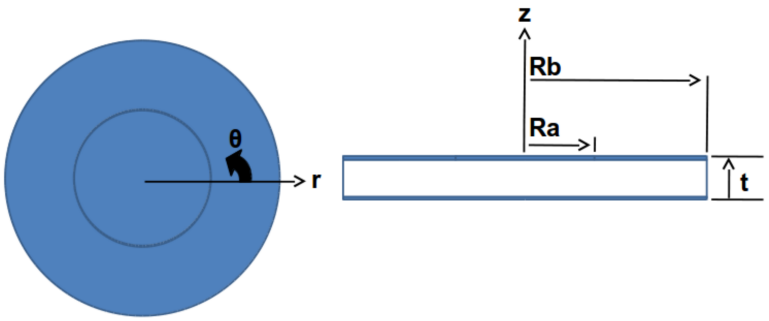

Figure 3.2: Schematic of Simplified Piezoelectric Disc Transformer used during Analytical Modeling, R_a and R_b are the outer Radii of the Output Circular Electrode and Input Annulus Electrode, Respectively

3.3 Analytical Disc PT Modeling via Extended Hamilton's Method

The Extended Hamilton's Principle (documented in Meirovitch's [108] and Reddy's [109] books) lends itself to the modeling of PTs due to the general nature of the theory. If expressions for the kinetic energy, potential energy and non-conservative work of the system can be formulated, the approach can derive all equations of motion in a relatively straightforward manner, irrespective of the type of physics involved. For example, PT modeling involves both mechanics (vibrations and mechanical work) and electrophysics (electrical work), and so benefits from just such an approach. For these reasons, this approach is adopted in the present work.

Equation 3.4 is written in terms of Cartesian coordinates, but is a constitutive equation of the system and therefore valid in any coordinate system. In the present problem we would like to use cylindrical coordinates, so we compare equivalent terms in equations 3.6 and 3.7. In order to use the electric enthalpy equation here,

we substitute equivalent terms from the cylindrical equations in for their Cartesian counterparts in 3.4, with the following result:

$$H = \frac{1}{2s_{11}^E(1-\nu^2)}\Big((S_r+\nu S_\theta)S_r + (\nu S_r + S_\theta)S_\theta\Big) \\ -\frac{d_{31}}{s_{11}^E(1-\nu)}E_z(S_r+S_\theta) - \frac{1}{2}\epsilon_{33}^T(E_z)^2 \tag{3.12}$$

This formulation of the electric enthalpy will be used to derive the analytical model considered here, and it will be shown that it can also re-derive the equation of motion of a piezoelectric disc, reviewed in the previous section.

The Generalized Hamilton's Principle can be stated as follows for an electromechanical system with piezoelectric components, from Eqn. 6.13 in Tiersten [104]:

$$\int_{t_1}^{t_2} (\delta L)\, dt = 0 \tag{3.13}$$

Where L is the Lagrangian energy formulation, defined by combining the kinetic energy of the disc, its electric enthalpy H (defined for the present work, above), and the virtual work done by surface tractions (not present here) and charges W, also from Tiersten:

$$L = \int_{Vol}\left(\frac{1}{2}\rho\dot{u}_r^2 - H\right) dVol + \int_{Area}(W)\, dArea \tag{3.14}$$

Substituting equations 3.12 and 3.3, we have the form to be used here, with Q_{Area} and V representing the surface charge per unit area, and voltage, respectively, on the surface of the device:

$$L = \int_{Vol} \left(\frac{1}{2}\rho \dot{u}_r^2 - \frac{1}{2s_{11}^E(1-\nu^2)} \Big((u_{r,r} + \nu \frac{u_r}{r}) u_{r,r} + (\nu u_{r,r} + \frac{u_r}{r}) \frac{u_r}{r} \Big) \right.$$
$$\left. + \frac{d_{31}}{s_{11}^E(1-\nu)} E_z (u_{r,r} + \frac{u_r}{r}) + \frac{1}{2} \epsilon_{33}^T (E_z)^2 \right) dVol - \int_{Area} (Q_{Area} V)\, dArea \tag{3.15}$$

Terms in equation 3.15 are evaluated separately in the following sections, with the usual assumption that the virtual displacements take place instantaneously (variations evaluated over $\Big|_{t_1}^{t_2} = 0$). The volume integral is defined as follows for this problem (R_b = radius of disc, 2π = one complete circumference, t = thickness):

$$\int_{Vol} dVol = \int_0^t \int_0^{2\pi} \int_0^{R_b} r dr d\theta dz = 2\pi t \int_0^{R_b} r dr \tag{3.16}$$

3.3.1 Kinetic Energy

The equation for the kinetic energy is:

$$\rho \pi t \int_0^{R_b} \dot{u}_r^2 r dr \tag{3.17}$$

and the variation of the kinetic energy is:

$$2\rho \pi t \int_0^{R_b} \dot{u}_r \delta \dot{u}_r r dr \tag{3.18}$$

followed by the extended Hamilton form:

$$
\begin{aligned}
&2\rho\pi t \int_{t_1}^{t_2}\int_0^{R_b} \ddot{u}_r \delta\dot{u}_r r dr dt \\
&= 2\rho\pi t \left(\dot{u}_r \delta u_r \Big|_{t_1}^{t_2} - \int_{t_1}^{t_2}\int_0^{R_b} \ddot{u}_r \delta u_r r dr dt \right) \\
&= -2\rho\pi t \int_{t_1}^{t_2}\int_0^{R_b} \ddot{u}_r \delta u_r r dr dt
\end{aligned}
\tag{3.19}
$$

3.3.2 Electric Enthalpy

$$
\begin{aligned}
H = \frac{\pi t}{s_{11}^E(1-\nu^2)} \int_0^{R_b} \left(u_{r,r}^2 + \frac{2\nu}{r} u_{r,r} u_r + \frac{u_r^2}{r^2} \right) r dr \\
-\frac{2\pi t d_{31}}{s_{11}^E(1-\nu)} \int_0^{R_b} \left(u_{r,r} + \frac{u_r}{r} \right) E_z r dr - \pi t \epsilon_{33}^T \int_0^{R_b} E_z^2 r dr
\end{aligned}
\tag{3.20}
$$

3.3.2.1 Re-Derivation of Disc Equations of Motion from Literature

At this point, it is important to note that if we take the variation of the equation above for the case of a vibrating piezoelectric disc (not a disc transformer) with constant applied E-field, $\delta E_z = 0$, so the last two terms fall out, and considering the variation of the surface charge is also zero, only terms from equations 3.19 and part of 3.20 are left. These terms are the exact disc equations of motion and boundary conditions mentioned earlier, where R is the outer radius of the disc (equations 3.8 and 3.10):

$$\begin{aligned}\int_{t_1}^{t_2}\delta\left(\int_{Vol}\left(\frac{1}{2}\rho\dot{u}_r^2-H\right)dVol+\int_{Area}(W)\,dArea\right)dt=\\ -2\rho\pi t\int_{t_1}^{t_2}\int_0^R\ddot{u}_r\delta u_r r dr dt\\ -\frac{2\pi t}{s_{11}^E(1-\nu^2)}\int_{t_1}^{t_2}\left(ru_{r,r}\delta u_r\Big|_0^R-\int_0^R\left(u_{r,r}+ru_{r,rr}\right)\delta u_r dr\right.\\ \left.+\nu\left(u_r\delta u_r\Big|_0^R\right)dr+\int_0^R\frac{u_r}{r}\delta u_r dr\right)dt\end{aligned}\tag{3.21}$$

To extract the equations of motion, the arbitrariness of δu_r is invoked and therefore the coefficients of δu_r are taken to equal zero, with the terms integrated over the entire disc representing the equations of motion, and the terms evaluated at 0 and R the boundary conditions:

$$-2\rho\pi t r\ddot{u}_r+\frac{2\pi t}{s_{11}^E(1-\nu^2)}\left(u_{r,r}+ru_{r,rr}-\frac{u_r}{r}\right)=0\tag{3.22}$$

$$\begin{aligned}\frac{1}{s_{11}^E(1-\nu^2)}\left(u_{r,r}+\nu\frac{u_r}{r}\right)\Big|_{r=R}=T_r\Big|_{r=R}^{\delta E_z=0}=0\\ u_r\Big|_{r=0}=0\end{aligned}\tag{3.23}$$

Rearranging Eqn. 3.22, with an assumed sinusoidally varying deflection $u_r = u_r(r)e^{j\omega t}$, where ω is the frequency of oscillation with time, we re-derive Eqn. 3.8:

$$\begin{aligned}u_{r,rr}+\frac{u_{r,r}}{r}+\omega^2\rho s_{11}^E(1-\nu^2)u_r-\frac{u_r}{r^2}\\ =u_{r,rr}+\frac{u_{r,r}}{r}+\left(\lambda^2-\frac{1}{r^2}\right)u_r=0\end{aligned}\tag{3.24}$$

3.3.3 Electric Enthalpy, Continued

Because the known disc equations and boundary conditions from the literature could be re-derived with the present method, additional confidence is gained in this approach. Continuing with the variation of the electric enthalpy, and including the following definitions for the electric field, where E_z is the electric field in the z-direction, R_L is the load resistance, Q_z is the electrical charge, and V_{in} is the input voltage:

$$\int_0^{R_b} E_z = \int_0^{R_a} \frac{R_L}{t}\dot{Q}_z + \int_{R_a}^{R_b} \frac{V_{in}}{t} \tag{3.25}$$

$$\begin{aligned} H = {} & \frac{\pi t}{s_{11}^E(1-\nu^2)} \int_0^{R_b} \left(u_{r,r}^2 + \frac{2\nu}{r} u_{r,r} u_r + \frac{u_r^2}{r^2} \right) r dr \\ & - \frac{2\pi t d_{31}}{s_{11}^E(1-\nu)} \Big(\int_0^{R_a} \left(u_{r,r} + \frac{u_r}{r} \right) \frac{R_L}{t} \dot{Q}_z r dr + \int_{R_a}^{R_b} \left(u_{r,r} + \frac{u_r}{r} \right) \frac{V_{in}}{t} r dr \Big) \\ & - \pi t \epsilon_{33}^T \Big(\int_0^{R_a} \frac{R_L^2}{t^2} \dot{Q}_z^2 r dr + \int_{R_a}^{R_b} \frac{V_{in}^2}{t^2} r dr \Big) \end{aligned} \tag{3.26}$$

The variation of the electric enthalpy is:

$$\begin{aligned} \delta H = {} & \frac{2\pi t}{s_{11}^E(1-\nu^2)} \int_0^{R_b} \Big(u_{r,r}\delta u_{r,r} + \nu \left(u_r \delta u_{r,r} + u_{r,r}\delta u_r \right) + \frac{u_r}{r}\delta u_r \Big) dr \\ & - \frac{2\pi t d_{31}}{s_{11}^E(1-\nu)} \Bigg(\frac{R_L}{t} \int_0^{R_a} \Big(r \left(\dot{Q}_z \delta u_{r,r} + u_{r,r}\delta \dot{Q}_z \right) + \left(\dot{Q}_z \delta u_r + u_r \delta \dot{Q}_z \right) \Big) \\ & + \frac{V_{in}}{t} \int_{R_a}^{R_b} \left(r\delta u_{r,r} + \delta u_r \right) dr \Bigg) \\ & - \frac{2\pi t \epsilon_{33}^T R_L^2}{t} \Big(\int_0^{R_a} \dot{Q}_z \delta \dot{Q}_z r dr + 0 \Big) \end{aligned} \tag{3.27}$$

and the extended Hamilton form is:

$$
\begin{aligned}
\int_{t_1}^{t_2} \delta H = \frac{2\pi t}{s_{11}^E(1-\nu^2)} \int_{t_1}^{t_2} \Bigg(& r u_{r,r} \delta u_r \Big|_0^{R_b} - \int_0^{R_b} \left(u_{r,r} + r u_{r,rr}\right) \delta u_r dr \\
& + \nu \left(u_r \delta u_r \Big|_0^{R_b} - 0 \right) + \int_0^{R_b} \frac{u_r}{r} \delta u_r dr \Bigg) dt \\
- \frac{2\pi t d_{31}}{s_{11}^E(1-\nu)} \Bigg(\frac{R_L}{t} \int_{t_1}^{t_2} \Big(& r \dot{Q}_z \delta u_r \Big|_0^{R_a} - \int_0^{R_a} \dot{Q}_z \delta u_r dr + 0 - \int_0^{R_a} r \dot{u}_{r,r} \delta Q_z dr \\
& + \int_0^{R_a} \dot{Q}_z \delta u_r dr + 0 - \int_0^{R_a} \dot{u}_r \delta Q_z dr \Big) dt \\
& + \int_{t_1}^{t_2} \frac{V_{in}}{t} \Big(r \delta u_r \Big|_{R_a}^{R_b} - \int_{R_a}^{R_b} \delta u_r dr + \int_{R_a}^{R_b} \delta u_r dr \Big) dt \Bigg) \\
& + \frac{2\pi t \epsilon_{33}^T R_L^2}{t} \int_{t_1}^{t_2} \int_0^{R_a} \ddot{Q}_z \delta Q_z r dr
\end{aligned}
\tag{3.28}
$$

3.3.4 Surface Charge

The variable for the surface charge with respect to area is represented as Q_{Area}, to avoid confusion with the absolute charge Q_z:

$$
\begin{aligned}
& - \int_{Area} \left(Q_{Area} V\right) dArea \\
= & - \int_0^{2\pi} \int_0^{R_a} \left(Q_{Area} V\right) r dr d\theta \\
= & -2\pi \int_0^{R_a} \left(Q_{Area} V\right) r dr
\end{aligned}
\tag{3.29}
$$

The variation of the surface charge is:

$$
\begin{aligned}
& \delta \Bigg(- \int_{Area} \left(Q_{Area} V\right) dArea \Bigg) \\
= & -2\pi \int_0^{R_a} \left(Q_{Area} \delta V\right) r dr
\end{aligned}
\tag{3.30}
$$

and the extended Hamilton form is, using the substitution $\delta V = R_L \delta \dot{Q}_z$:

$$\begin{aligned}\int_{t_1}^{t_2}\Big(-2\pi\int_0^{R_a}\Big(Q_{Area}R_L\delta\dot{Q}_z\Big)\,rdr\Big)dt \\ = 0 + 2\pi R_L\int_{t_1}^{t_2}\int_0^{R_a}\dot{Q}_{Area}\delta\dot{Q}_z r dr dt\end{aligned} \tag{3.31}$$

3.3.5 Disc PT Equations of Motion

By substituting equations 3.19, 3.28 and 3.31 into 3.13, we assemble the equations of motion:

$$\begin{aligned}&-2\rho\pi t\int_{t_1}^{t_2}\int_0^{R_b}\ddot{u}_r\delta u_r r dr dt \\ &-\frac{2\pi t}{s_{11}^E(1-\nu^2)}\int_{t_1}^{t_2}\Bigg(ru_{r,r}\delta u_r\Big|_0^{R_b}-\int_0^{R_b}\left(u_{r,r}+ru_{r,rr}\right)\delta u_r dr \\ &\qquad+\nu\left(u_r\delta u_r\Big|_0^{R_b}\right)+\int_0^{R_b}\frac{u_r}{r}\delta u_r dr\Bigg)dt \\ &+\frac{2\pi t d_{31}}{s_{11}^E(1-\nu)}\Bigg(\frac{R_L}{t}\int_{t_1}^{t_2}\Big(r\dot{Q}_z\delta u_r\Big|_0^{R_a}-\int_0^{R_a}r\dot{u}_{r,r}\delta Q_z dr \\ &\qquad-\int_0^{R_a}\dot{u}_r\delta Q_z dr\Big)dt+\int_{t_1}^{t_2}\frac{V_{in}}{t}\Big(r\delta u_r\Big|_{R_a}^{R_b}\Big)dt\Bigg) \\ &-\frac{2\pi t\epsilon_{33}^T R_L^2}{t}\int_{t_1}^{t_2}\int_0^{R_a}\ddot{Q}_z\delta Q_z r dr+2\pi R_L\int_0^{R_a}\dot{Q}_{Area}\delta\dot{Q}_z r dr=0\end{aligned} \tag{3.32}$$

To extract the equations of motion, the arbitrariness of δu_r and δQ_z (the degrees of freedom to be solved for) is invoked, and their coefficients represent the equations of motion and boundary conditions as follows.

For the radial mechanical deflection degree of freedom, u_r, with an assumed sinusoidally varying deflection $u_r = u_r(r)e^{j\omega t}$:

$$u_{r,rr} + \frac{u_{r,r}}{r} + \left(\lambda^2 - \frac{1}{r^2}\right) u_r = 0 \tag{3.33}$$

with:

$$\lambda^2 = \omega^2 \rho s_{11}^E (1 - \nu^2) \tag{3.34}$$

For the electrical degree of freedom, Q_z:

$$\begin{aligned} \frac{-2\pi d_{31}}{s_{11}^E(1-\nu)} \left(R_L \left(r\dot{u}_{r,r} + \dot{u}_r \right) \right) - \frac{2\pi \epsilon_{33}^T R_L^2}{t} r\ddot{Q}_z \\ +2\pi r R_L \dot{Q}_{Area} = 0 \end{aligned} \tag{3.35}$$

With an assumed sinusoidally varying charge $Q_z = Q_z(r)e^{j\omega t}$ and deflection $u_r = u_r(r)e^{j\omega t}$, cancelling common terms, multiplying by the output area πR_a^2 and substituting $R_L \omega Q = V$:

$$\frac{-d_{31} R_L \omega (\pi R_a^2)}{s_{11}^E (1-\nu)} \Big(r u_{r,r} + u_r \Big) j + \frac{\epsilon_{33}^T R_L \omega (\pi R_a^2)}{t} r V_{out} + r V_{out} j = 0 \tag{3.36}$$

and solving for V_{out}, the voltage at the output electrode:

$$V_{out} = \frac{\frac{d_{31} R_L \omega (\pi R_a^2)}{s_{11}^E (1-\nu)} \Big(r u_{r,r} + u_r \Big) j}{r \left(j + \frac{\epsilon_{33}^T R_L \omega (\pi R_a^2)}{t} \right)} \tag{3.37}$$

The boundary conditions are as follows:

$$
\begin{aligned}
\frac{2\pi t}{s_{11}^E(1-\nu^2)}\left(ru_{r,r}\Big|_{r=0}+\nu u_r\Big|_{r=0}\right)-\frac{2\pi d_{31}}{s_{11}^E(1-\nu)}\left(R_L r\dot{Q}_z\Big|_{r=0}\right)&=0\\
\therefore \qquad u_r\Big|_{r=0}&=0\\
\frac{2\pi d_{31}}{s_{11}^E(1-\nu)}\left(R_L r\dot{Q}_z\Big|_{r=R_a}-V_{in}r\Big|_{r=R_a}\right)&=0\\
\therefore \qquad V_{out}=V_{in}\Big|_{r=R_a}&\\
\frac{-2\pi t}{s_{11}^E(1-\nu^2)}\left(ru_{r,r}\Big|_{r=R_b}+\nu u_r\Big|_{r=R_b}\right)+\frac{2\pi d_{31}}{s_{11}^E(1-\nu)}\left(V_{in}r\Big|_{r=R_b}\right)&=0\\
\therefore \qquad T_r\Big|_{r=R_b}&=0
\end{aligned}
\tag{3.38}
$$

3.3.6 Solving Equations of Motion

In order to predict the voltage gain performance of a disc transformer, the first step is to solve equation 3.33 for u_r, and then substitute u_r into the voltage equation 3.37. Rogacheva has proposed a solution to equation 3.33 for several different configurations, including partially and fully electrode covered discs [65]. She uses the following three boundary conditions to set up a system of equations for a partially electroded disc (input annulus electrode only), to be solved for the unknown Bessel function constants, where superscripts denote unelectroded (un) and electroded (e) sections of the device:

$$
\begin{aligned}
u_r^{un}\Big|_{r=R_a}&=u_r^{e}\Big|_{r=R_a}\\
T_r^{un}\Big|_{r=R_a}&=T_r^{e}\Big|_{r=R_a}\\
T_r\Big|_{r=R_b}&=0
\end{aligned}
\tag{3.39}
$$

In the present work the last boundary condition will be modified to include the effect of mechanical tethering on the outer radius of the disc. The present work considers a partially electrode covered disc model due to the system consisting of an input electrode annulus, surrounding a circular output electrode (to simplify the solution method, the gap between input and output electrodes is neglected, as seen in figure 3.2). The outer annulus motivates the disc's movement through an input voltage, and the inner output electrode provides some damping to the system by extracting energy and delivering it to an external load, so Rogacheva's solution will be used to approximate the solution for the device performance.

Numerical model output can be compared to analytical output, and when both methods report similar results, higher confidence can be attributed to those results. FEA models of this system contribute to comparisons seen in figures 3.3 and 3.12. Please see Appendix A for more information about numeric and analytic codes.

Figure 3.3 shows the normalized forced deflection for a 4mm disc PT calculated by the analytical model without mechanical tethers, compared to a FEA disc model forced deflection without tethers. Both predict the region from the center to roughly the edge of the output electrode undergoes linear deflection, while the region underneath the input annulus shows nonlinear deflection. The fundamental difference between the analytical and FEA models is that the analytical model assumes purely radial deflection (see section 3.2), while the FEA model is not constrained to purely radial modes, and is able to predict the influence of other modes, be they real or non-physical (spurious [110]). Even when comparing only radial mode results from FEA predictions to analytical radial mode results, there are still

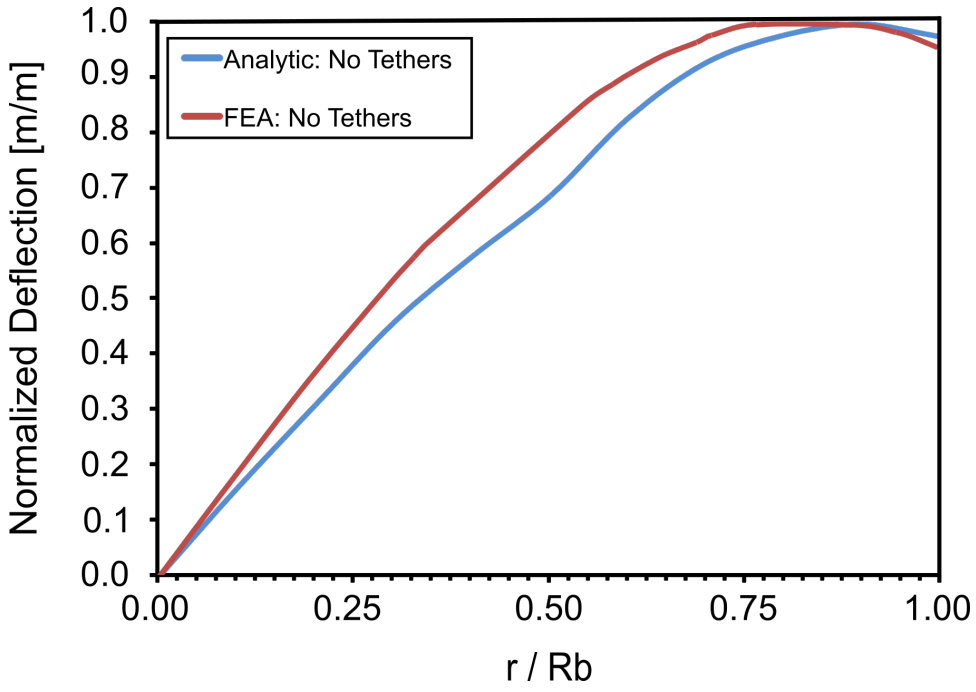

Figure 3.3: Normalized Forced Deflection versus Normalized Disc Radius, Analytical Model vs. FEA for a 4mm Diameter AR4 Disc PT. Both models show the same trend, but are not exactly equivalent, due to different assumptions made during modeling, and potentially different methods of problem solution.

some differences in prediction between models. These differences in predicted gain are likely due to different assumptions made in each model and potentially different methods of solution, but the methods of solution cannot be compared because the FEA method of solution is not readily available. However, results from both models are consistent in their overall trends, and are a good compliment to one another.

3.3.6.1 Tether Stiffness

Experimental and predictive results indicate that tethering has a significant impact on device performance, and in this section the mathematical treatment of

tethers using the Extended Hamilton approach will be discussed. In order to investigate the difference in performance observed between tethered and untethered devices, the analytical model can be modified to account for the stiffness and mass of device tethers, by modeling them as massive springs that act on the outer radius of the device. This is only an approximation of their actual behavior, but is still useful from a device design perspective. To make the model more realistic, the mass of the springs will be included, in addition to the stiffness, which is important when considering very compliant tethers, physically necessitating large folded flexure elements. The mass of the springs $\bar{m}$ is proportional to the length of the longest folded beam tether element l_k ($\bar{m} \propto l_k$), and their stiffness is proportional to the inverse cube power of l_k ($k \propto \frac{1}{l_k^3}$) (Castigliano's Method); rearranging these relationships leads to an inverse relationship between mass and the cube root of tether stiffness ($\bar{m} \propto \frac{1}{\sqrt[3]{l_k}}$). In this way tether stiffness can be used in numeric calculations to determine the boundary condition created by tethering. The expected behavior is that as tethers approach high levels of stiffness, disc motion will be restricted and gain will decrease, and at the other extreme, the added mass of compliant tethers will also reduce performance, leading to an optimum point of performance at an intermediate stiffness value.

First, the system Lagrangian should be modified to include the potential and kinetic energy terms for the spring, L_k:

$$L = \int_{Vol} \left(\frac{1}{2} \rho \dot{u}_r^2 - H \right) dVol + L_k + \int_{Area} (W)\, dArea \tag{3.40}$$

where $L_k = T_k - V_k$ is defined for the two microfabricated tethers with assumed identical stiffness k and mass $\bar{m}$. In this model the tethers are assumed to provide a boundary condition symmetrically constraining the device motion on the periphery of the device, which is justified due to the uniform radial extension mode behavior of the disc.

$$L_k = \left(\frac{1}{2} \left(\bar{m} \dot{u}_r^2 - k u_r^2 \right) \right) \Big|_{r=R_b} \tag{3.41}$$

The variation of L_k is:

$$\delta L_k = \left(\bar{m} \dot{u}_r \delta \dot{u}_r - k u_r \delta u_r \right) \Big|_{r=R_b} \tag{3.42}$$

and Extended Hamilton form:

$$\int_{t_1}^{t_2} \delta L_k dt = \int_{t_1}^{t_2} \left(-\bar{m} \ddot{u}_r - k u_r \right) \delta u_r dt \Big|_{r=R_b} \tag{3.43}$$

Therefore, the boundary conditions, equation 3.38, would have the following difference:

$$\frac{-2\pi t}{s_{11}^E (1-\nu^2)} \left(r u_{r,r} \Big|_{r=R_b} + \nu u_r \Big|_{r=R_b} \right) + \frac{2\pi d_{31}}{s_{11}^E (1-\nu)} \left(V_{in} r \Big|_{r=R_b} \right) - \left(\bar{m} \ddot{u}_r + k u_r \right) \Big|_{r=R_b} = 0$$

$$\therefore \qquad T_r \Big|_{r=R_b} = - \frac{\bar{m} \ddot{u}_r + k u_r}{2\pi t r} \Big|_{r=R_b} \tag{3.44}$$

When this change in boundary conditions is implemented, the analytic model can be interrogated to determine the relationship between gain and tether stiffness, see figure 3.4. Please see Matlab code in Appendix A.

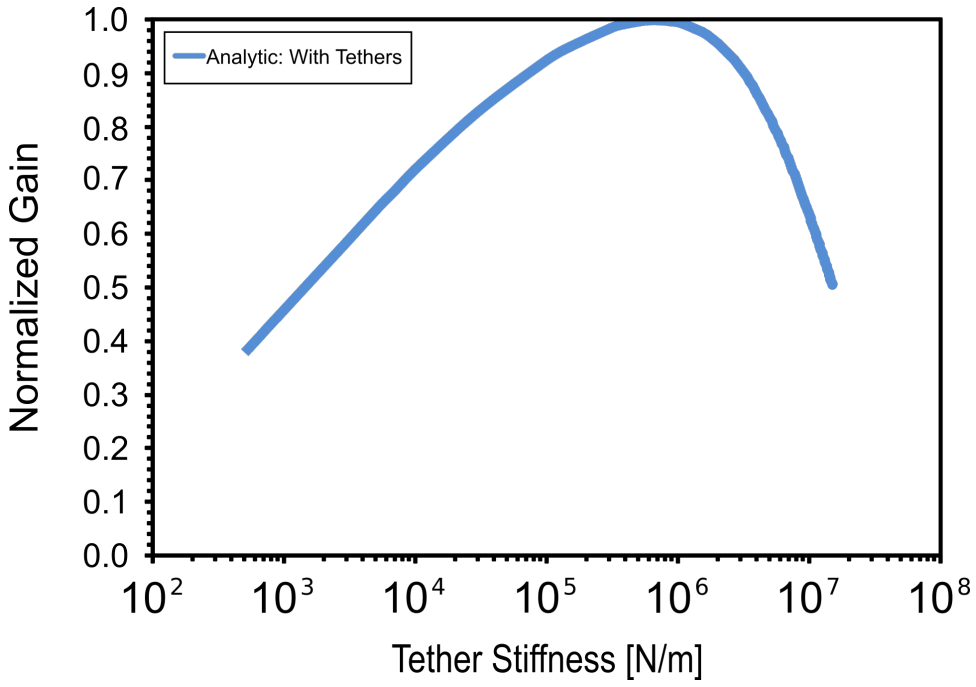

Figure 3.4: Analytical normalized gain prediction of AR4 disc PT for varying folded beam tether stiffness. Gain decreases at lower values of stiffness due to high mass loading associated with large, compliant folded beam tethers, and gain also decreases at high stiffness values due to increased tether stiffness restricting device motion. Optimum gain is predicted between 10^5 - 10^6N m^{-1}; therefore as-designed tethers in this work achieve near maximum theoretical performance at 232KN m^{-1}.

3.3.6.2 Damping

Possible sources of damping in this work include acoustic damping as device movement displaces surrounding air, and internal material inefficiencies (material damping). Due to the size scale of the devices in question, and the fact that they are resonating in-plane, air damping was assumed to be negligible compared to internal material damping. This was verified by FEA analysis using a surrounding air domain (see figure 3.6) and analytical analysis using the approach in [111]. Fast-moving (100s of kHz) structures in air are expected to have low levels of damping, and the present work matches that expectation as predicted by Couette values on the order of $\frac{1}{Q} \propto 10^{-7}$, for a 4mm diameter device resonating at 550 kHz [111]. Material damping is orders of magnitude larger than air damping in the present work.

Material damping was implemented in both FEA and analytical models via imaginary complex material constants [112, 113], with the isotropic loss factor (inverse of quality factor) for compliance damping η and the dielectric damping factor δ defined as:

$$\begin{aligned} \eta &= \frac{1}{Q} \\ \delta &= \frac{1}{\sqrt{1 - k_{31}^2}} - 1 \end{aligned} \tag{3.45}$$

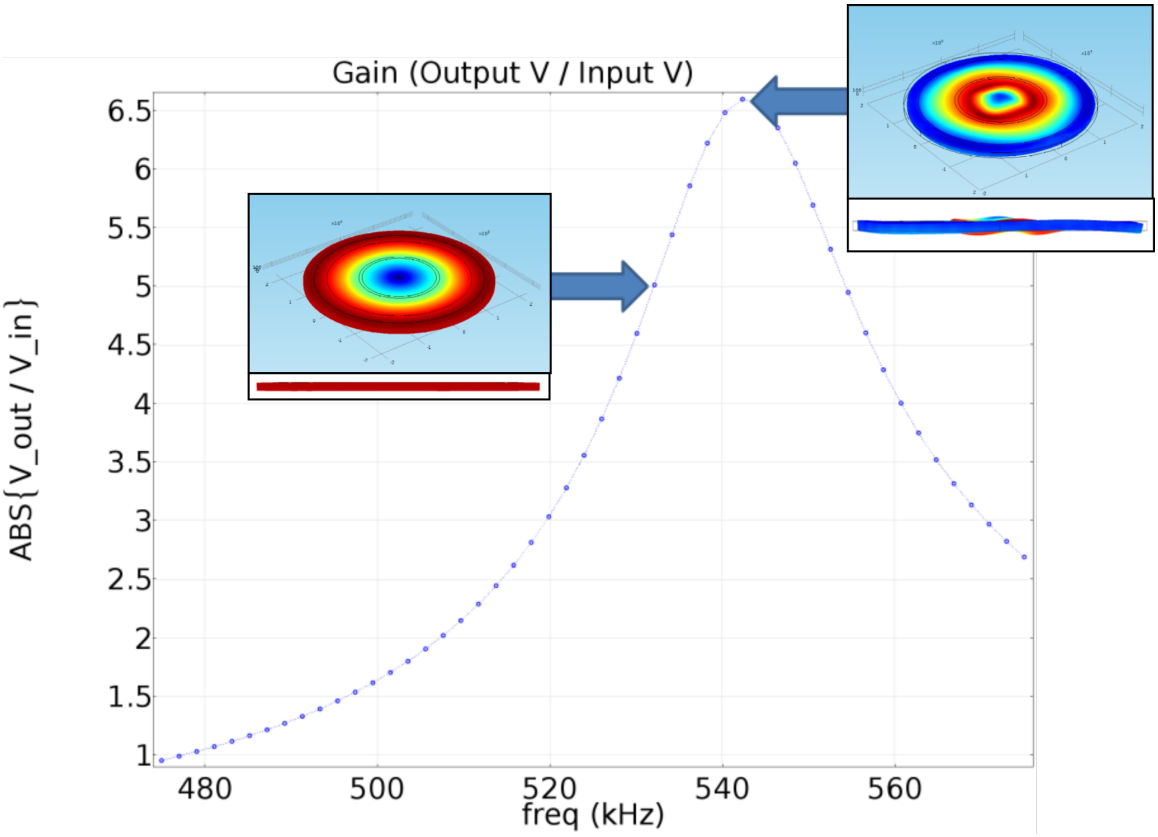

Figure 3.5: FEA frequency sweep at 1MΩ load for an untethered AR4 4mm diameter disc transformer. The highest gain predicted is associated with out-of-plane bending modes (as shown by inset figure at 542 kHz), but the highest gain predicted for fundamental resonance (as shown by inset figure at 533 kHz) is much closer to experimental results; FEA results were interpreted in this way in the present work (Figure 3.12).

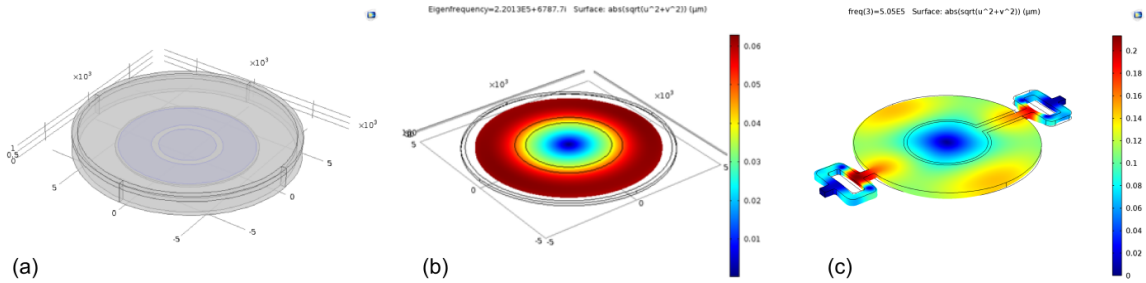

Figure 3.6: (a) FEA Model of ideal circular geometry (scaled in μm), surrounded by an air domain for acoustic damping simulations (which proved that acoustic damping has little to no effect on radial mode operation at these device scales); (b) Eigenfrequency analysis of a 10mm diameter, 0.127mm thick round PZT disc, showing radial extension; (c) As-fabricated 4mm diameter tethered device geometry, for comparison with experimental results (predicted radial expansion in μm and [exaggerated, for clarity] radial deflection is shown).

3.4 Numeric Disc PT Modeling

FEA simulations were also used to predict device performance. Devices were operated near fundamental resonance frequencies for optimal performance, as determined experimentally through maximizing gain. FEA simulations predicted that maximum gain conditions could occur slightly above or below fundamental resonances, depending on impedance conditions of device and load, but this was not experimentally verified (e.g. through laser doppler vibrometry).

Examples of simulation output can be seen in Figures 3.5, 3.6 and 3.7. FEA models accurately predicted device resonance frequency, as seen in Table 3.2. FEA model predictions correlated extremely well with experimental results for 1kΩ output loads and lower, giving confidence that the desired modes were being excited in

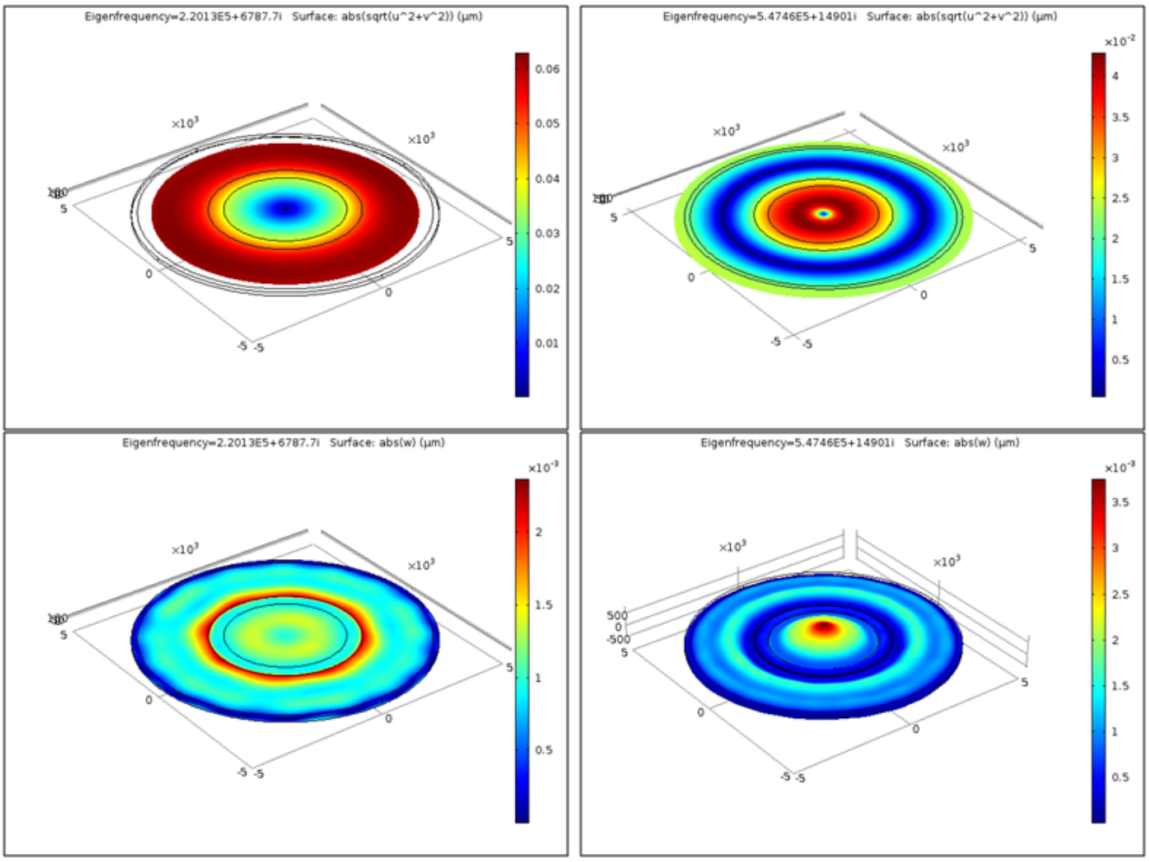

Figure 3.7: FEA eigenfrequency model of ideal circular 10mm diameter disc, predicting the natural frequencies of the first radial expansion mode of 220kHz and of the second radial expansion mode of 547kHz. FEA and analytical models predicted experimental resonance frequencies accurately, generally with between 1% - 5% accuracy. Radial expansion is shown in the top images. Note that the first mode has only one node point in the center of the disc (blue section) and the second mode has two node points, as expected. The bottom row of images shows out-of-plane (z) displacement, which is one order less than radial displacement, matching the assumption that the ideal unforced fundamental and second radial mode vibration should primarily be in-plane.

Table 3.2: FEA Maximum Gain Frequency Predictions for Tethered Transformers and Experimental Results (Note: Maximum Gain Does Not Always Occur Exactly at Fundamental Mode Resonance Frequency, but Usually Falls Within 5% of Fundamental Frequency)

Device Diameter $[mm]$	Area Ratio $[Input/Output]$	Experimental Frequency $[kHz]$	FEA Model $[kHz]$	Error [%]
4	1	555	550	1
4	2	546	539	2
4	3	540	534	2
4	4	538	533	1

the experimental devices. At values of impedance greater than 1kΩ, FEA models predicted much higher maximum gain than either analytical modeling or experimental results. Figure 3.5 shows a FEA frequency sweep at 1MΩ load for an untethered disc transformer. The highest gain predicted is associated with out-of-plane bending modes (as shown by right inset figure), but the highest gain predicted for fundamental resonance is much closer to actual results (left inset figure). The out-of-plane modes predicted in FEA simulations were spurious based on comparison with analytical modeling and experimental results. Analytical models were based on purely radial motion (other modes were not possible), and they correlated more closely to experimental results at 1MΩ than FEA models with additional modes. Spurious modes in numerical simulations can result from excessively compliant systems, such as the untethered disc which is not constrained at its periphery, and this point has been studied previously [110]. In the present work, reported FEA results were taken from only the highest predicted fundamental radial mode gains, ignoring results as-

sociated with out-of-plane modes, and there was good correlation between these results and experimental results.

3.5 Results

3.5.1 Microfabrication Results

Prototype microfabrication results reported here can be seen in Figures 3.8 and 3.9. Folded beam flexure tethers were designed with rounded edges in order to eliminate possible stress concentrations and facilitate fabrication. Tethers were 200μm wide with a total length of 1,400μm across the long dimension of the tether, with 300μm gaps between attachment points. These dimensions were balanced between a desire to create thin tethers, a need to reliably microfabricate them within the manufacturing tolerances of our processes, and an attempt to achieve a beneficial mass-to-stiffness ratio (see figure 3.4). Folded beam tether stiffness was estimated using Castigliano's approach (as shown in [102]) to be 232kN m^{-1}.

3.5.2 Device Performance Results

The key results are summarized in: Figure 3.10, which shows an overview of the performance of prototype devices fabricated in the present work; Figure 3.11, which shows that the optimal area ratio varies with load; and Figure 3.12, which presents an analysis of the effect of device tethering on gain performance, along with FEA and analytical model verification.

Figure 3.10 gives an overview of 4mm diameter device performance for pro-

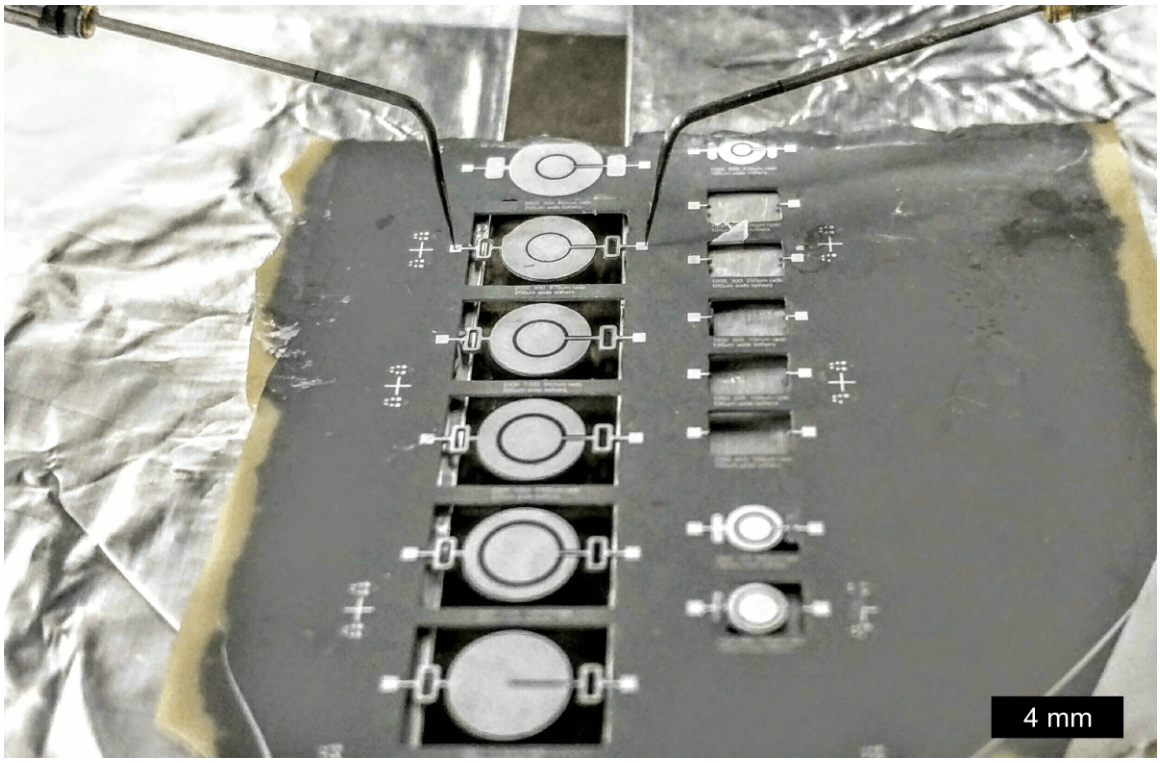

Figure 3.8: 4mm diameter tethered PZT transformers during testing. Input probe is seen on the left, and output probe on the right. As-fabricated area ratios of the released devices are 4, 3, 2, 1 and 1039, respectively, from the top. Only results from AR = 4,3,2,1 were reported here; AR = 1039 performed poorly.

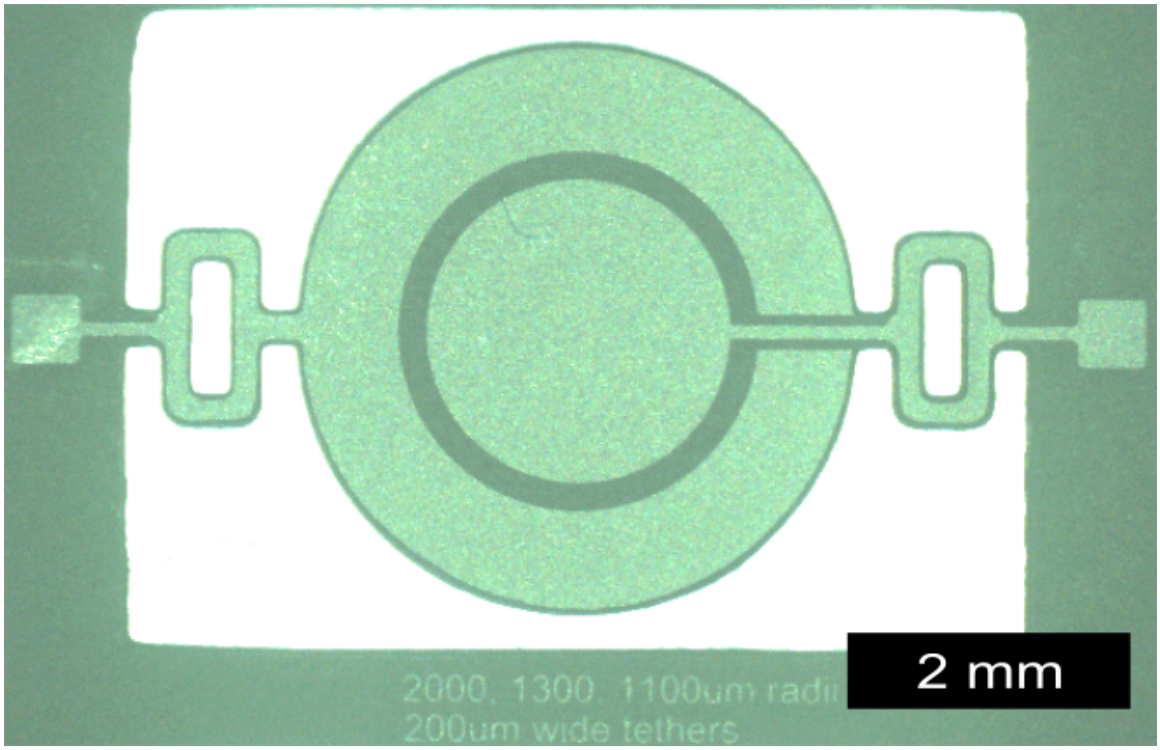

Figure 3.9: 4mm diameter tethered PZT transformer optical image. Resonating disc and tethers were fully released during powderblasting and Al metal covers almost the entire surface of the tethers, creating a reliable (redundant, in case either the top or bottom tether trace is damaged) electrical connection between the disc and the rectangular probe tip pads used for interfacing with the device.

totypes of different area ratio. Using the test procedure outlined in Section 2.2, voltage gain, output power and efficiency of the bulk transformers under varying electrical loads were recorded. The devices, with volume on the order of .002cm^3, several orders smaller than the bulk PT literature, showed peak gains across various prototypes of 2.6, efficiencies of 33% and output power of 80mW, for 3V-6V input voltage. Overall, experimental results and gain predictions from the tethered PT FEA model showed similar trends for lower output impedance values (roughly equivalent to the output impedance of the devices under test, measured to be between 1,000-5,000Ω using a LCR meter (Agilent 4284A) and ϵA d^{-1} calculations). At higher output loads the predictions were not as accurate, matching the behavior seen in the bulk PT literature. Number of measurements was marked $n = x$, and error bars shown are to one standard deviation.

Figure 3.12 displays voltage gain versus electrical load for area ratio (input area / output area) 4 disc transformers with and without tethers, along with model predictions. This chart reveals the effect that tethering has on device gain by comparing experimental results of prototypes with the same area ratio electrode configuration, but fabricated with and without tethers. Tethered devices in this comparison achieve approximately half the voltage gain of untethered discs at high values of load impedance, but the difference is less pronounced at impedances of 1kΩ and below.

Figure 3.12 also reveals that modeling results closely approximated device behavior for both tethered and untethered devices overall; however, in certain cases one model or the other more closely matched experimental results, leading to different insights. For example, as previously mentioned in Section 3.4, at higher electrical

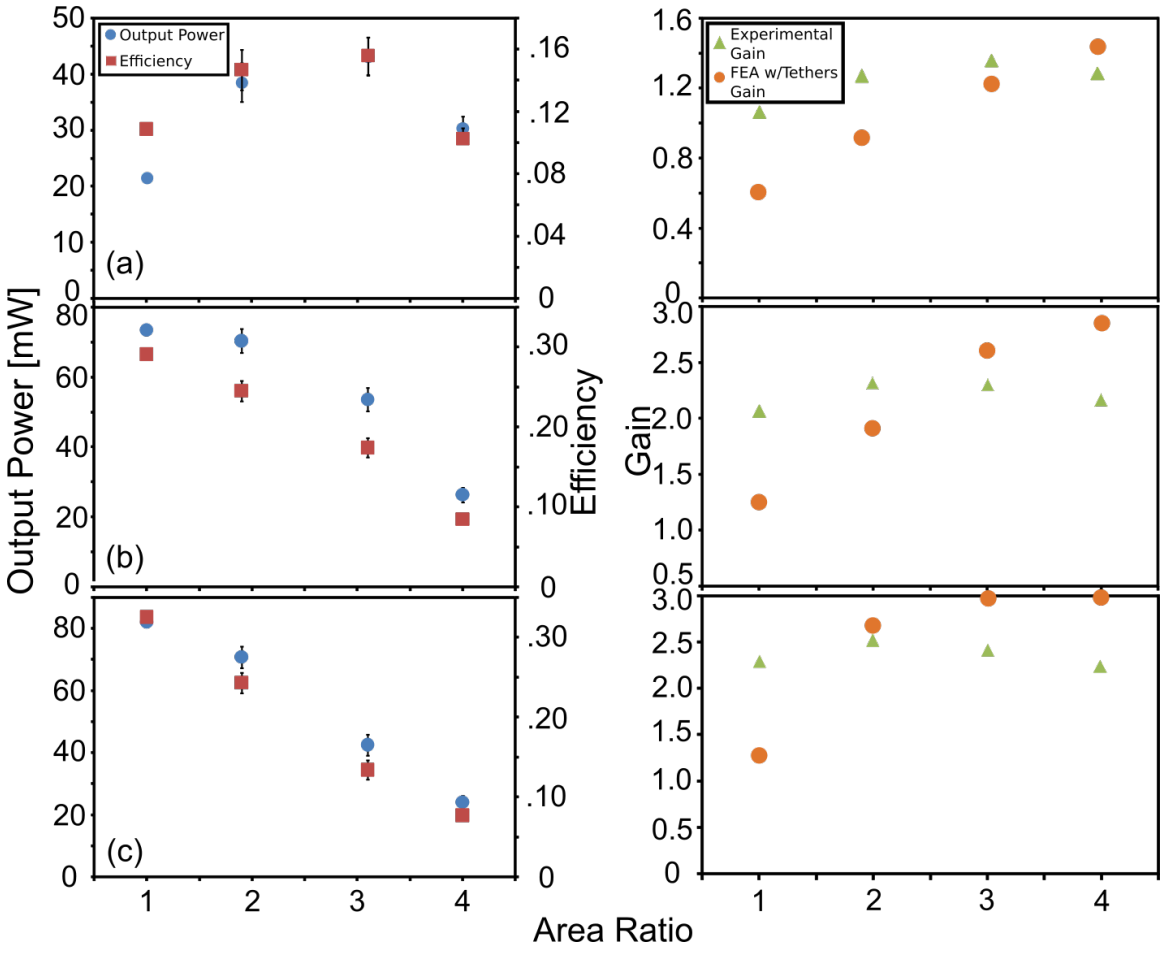

Figure 3.10: (a) Experimental output power and efficiency (left chart) and experimental vs. FEA predictive gain (right chart) for 4mm diameter devices of varying area ratio, with 1kΩ load. (b) With 10kΩ load (c) With 1MΩ load (n=3 trials from a single device in each chart). As seen in the literature, FEA predicts higher gain progressively for higher area ratios, while experimental results do not follow this trend. Reasons for model and experimental gain mismatch are discussed in Section 3.5.2.

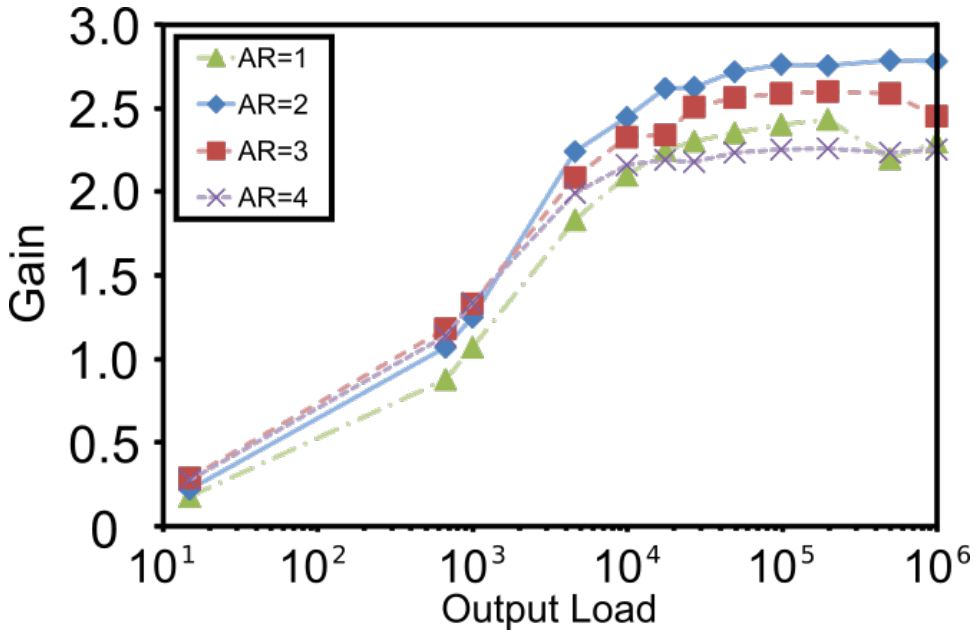

Figure 3.11: Experimental gain for 4mm diameter, area ratio (AR) = 1, 2, 3, 4 transformers vs. load impedance, showing gain increasing with increasing load, and AR = 2 device with the highest reported gain under high loading (n=3 trials from a single device in each data set). This chart shows that the optimal area ratio for maximizing gain varies with load, and that all devices follow a common trend as load increases. Lines added to guide the eye. Gain trend over decades of load impedance matches results from the literature, typical of piezoelectric voltage transformers.

load values analytical models more closely matched experimental results, leading to the determination that spurious modes were present in the FEA solution, and therefore leading to more accurate interpretation of FEA results. Also, regarding untethered discs, FEA modeling was more accurate at lower load values, most likely due to differences in model assumptions (such as including a gap between input and output electrodes in the FEA model, which more closely matches the real devices), and potentially also due to less constraints on the (idealized, radial-mode) analytic model. When considering device tethering, the analytic model (using spring elements with calculated stiffness of 232KN m^{-1}) predicted a greater negative effect on gain performance than the FEA model, due to the different boundary conditions in each model, and more closely matched experimental results. The satisfactory behavior of the analytic model also validates the Extended Hamilton approach to piezoelectric device modeling, based on the electric enthalpy, and gives confidence that this approach can be used for other unrelated piezoelectric problems as well.

Considering untethered disc transformer results, neither model exactly matches the experimental data at higher values of load impedance; however, this is also the case in the literature. A number of PT researchers have reported that analytical and FEA models become less accurate as output loads increase over 1kΩ [47, 72, 114]. Various hypotheses for this discrepancy are given, from incorrect material properties to different assumptions about damping, and there is no consensus in the literature. One potential hypothesis is that these discrepancies could be due to nonlinearities that become non-negligible as load increases, due to voltage increasing at the output of the device. Potential nonlinearities, combined with device material properties

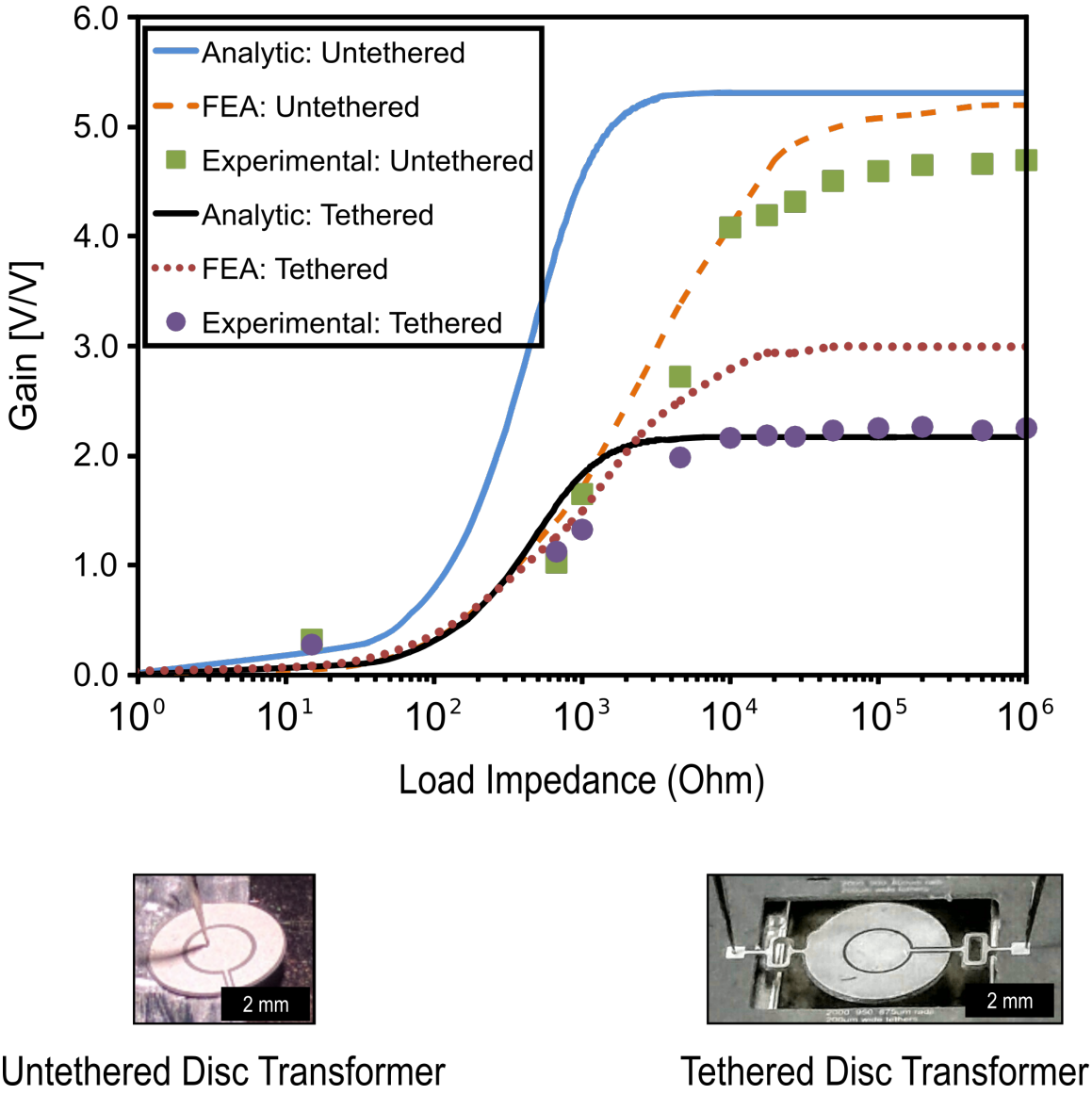

Figure 3.12: Analytical gain predictions compared with experimental results and numeric predictions: tethered and untethered 4mm diameter AR4 disc PTs. The fundamental difference between analytical and FEA predictions is that analytical modeling assumes only radial mode excitation, and FEA models incorporate many non-radial modes (either physical or spurious). Analytical tethered results predict experimental data more closely than FEA tethered results due to different treatment of the boundary condition associated with device tethers (see section 3.3.6.1) (n=3 trials from a single device in each data set).

that are either less than ideal or are estimated because they are not available from the manufacturer, could lead to significant discrepancies between predicted and experimental results. Most FEA and analytical models, including the ones in this work, are based on the linear theory of piezoelectricity, which could be a concern in cases of high voltage/load/temperature where the materials behave differently. Researchers are studying this phenomenon and have reported experimental validation of piezoelectric nonlinearities [25, 91–96].

The results presented here are similar to several larger (but lower-power) macro-scale devices in terms of gain and power handling, but efficiencies are lower than most macro-scale devices, which can partially be attributed to device tethering. The literature on bulk devices does not address tethering methods, or varying stiffness of tethers. Therefore the results in this work cannot be directly compared to other previous work. Also, some macro-scale devices were designed to handle Watts of power, which is not the case with the present work, which is intended to target micro-robotic and other small-scale applications.

Tethering vibrating disc transformers at their periphery, the location of greatest movement during fundamental radial extension, appears to degrade performance, and changes in tether design or creative manufacturing solutions to provide tethering at a different location could help improve performance. For example, fundamental resonance modes have a node location at the center of the device, and devising a method to constrain devices at this location could boost performance, but might not be compatible with traditional microfabrication techniques. A different device topology, length extensional free-free beams, is investigated in Chapter 4, which

addresses this concern by tethering at node locations that theoretically remain stationary during device resonance.

Based on the manufacturer's data, PZT 5A typically exhibits a mechanical quality factor of 80. Using a Network Analyzer (HP 4395A) in B/R (network) mode and the -3 dB method, a quality factor of 23 was measured for the 4mm diameter tethered transformers (30 for untethered), which was lower than the manufacturer's reported ideal material value likely due to factors such as mechanical tethering and device geometry.

10mm diameter untethered disc transformers were also manufactured by another graduate student, Mona Mirzaei, and tested in this work for modeling and testing procedure verification. As seen in Figure 3.13, a large range of area ratios, up to 60, were fabricated and tested. These results show more variability because they were not tested with an additional buffering circuit between the circuit under test and the oscilloscope probe, a practice used in all other measurements in the present work. These results also reinforce the trend seen in the present work, and the literature, that models become less accurate as electrical load increases.

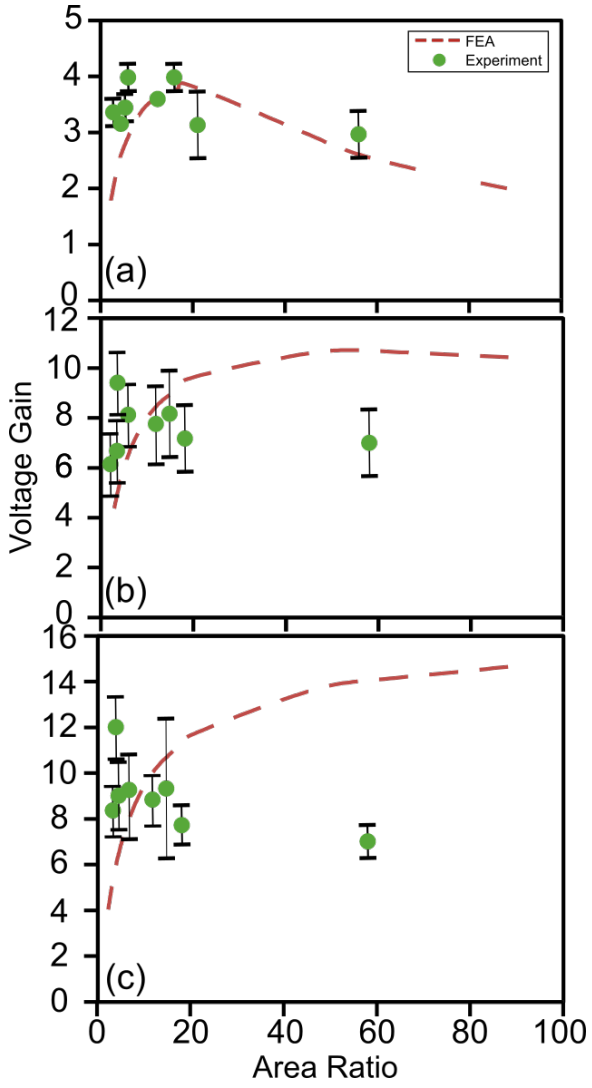

Figure 3.13: 10mm diameter, 0.127mm thick, PZT-5A untethered disc transformer gain vs. area ratio, experimental results and FEA predictions for: (a)1kΩ, (b)10kΩ, and (c)1MΩ load impedance. 10mm disc transformers were manufactured by another graduate student, Mona Mirzaei, and tested in this work for FEA model and testing setup verification. FEA predictions showed greater accuracy at lower values of output impedance, across multiple area ratio devices, matching other results in the present work and the literature. In general, analytical and FEA models are less accurate at higher values of load impedance, which is discussed in section 3.5.2 (n=3 trials from a single device in each chart).

Chapter 4: Rectangular Free-Free Beam PTs

4.1 Introduction

In addition to the circular topology investigated in Chapter 3, "free-free" beam topology, a rectangular cantilevered structure supported at its midsection across the narrow dimension, and free at opposite sides of its long dimension to vibrate [38], was also investigated. This design has the advantage that during in-plane length extensional vibration modes, the free ends' movement is unrestricted, and the structure can be supported at stationary node locations. For example, during the fundamental length extensional mode, there is one node point at the center of the beam (with respect to the long dimension). If the beam's tethers are located at this point, they will minimally oppose its desired motion, and straight, short tethers will be able to support the device during operation while not impeding its motion and allowing for a small total device footprint. This is in contrast to the radial designs presented in Chapter 3, which were tethered at the location of greatest deflection (the outer rim of the disc), and therefore required extensive design and analysis. Due to these factors, free-free designs may have improved performance for the same device volume, compared to radial designs, and were investigated in the same manner with respect to fabrication and testing.

4.2 Prior Work

Free-free beam devices were investigated on the micrometer scale by Bedair et al. [38, 115]. Different device modes were targeted and electrode geometries considered. Their findings include determining that if voltage gain is desired, the total input area of all input electrodes should be greater than the output area of all output electrodes, which has been confirmed in this work (see Section 4.3). Also, they determined that higher transformation ratios can be achieved by stacking device layers, which is more easily done with bulk PTs, but is fabrication intense with thin-film devices - showing one potential advantage to bulk devices compared to thin-film devices. Experimental reported results were a gain of 5.7 and <5% efficiency at 100kΩ load and a gain of 2 at almost 60% efficiency and 150Ω load (Figure 11 [38]).

Based on the previous work, a free-free beam design that has two input electrodes and one output electrode was considered here, and analytical and FEA models were developed to guide further design. A three electrode arrangement on the top side of the beam devices was designed to maximize voltage gain, with two exterior input electrodes and one interior output electrode; the converse electrode arrangement was simulated with FEA (one input and two output) but lower gain was predicted, so two exterior input electrodes and one central output electrode was selected as the operating design for all devices.

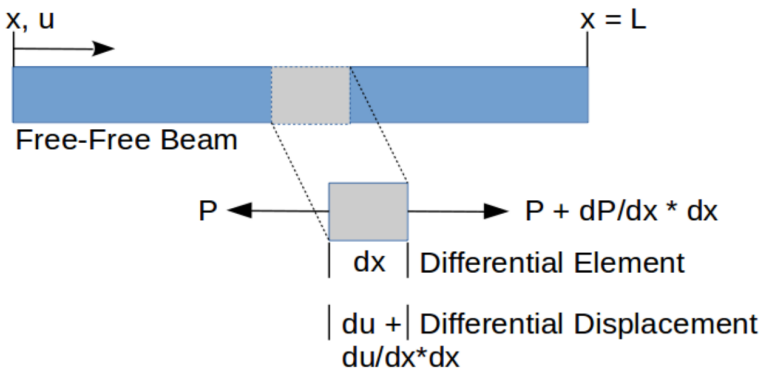

Figure 4.1: Free-Free Beam Diagram

4.3 Analytical and Numerical Modeling of Free-Free Beam PTs

The following is a mathematical derivation of the operation of a free-free beam resonator vibrating at its first longitudinal extension mode, based on a standard mathematical model of a free-free beam with axial loading [116]. This work is not original, and is re-derived here for completeness. Due to the straightforward nature of this device, additional modeling based on the Extended Hamilton Method (as done in Chapter 3) was not needed here.

With axial load P oriented in the positive x-direction, forces in the x-direction can be summed:

$$\sum F_x = P + \frac{\partial P}{\partial x}dx - P = m\frac{\partial^2 u}{\partial t^2} \tag{4.1}$$

$$\frac{\partial P}{\partial x}dx = m\frac{\partial^2 u}{\partial t^2} \tag{4.2}$$

Strain is defined as $\frac{\partial u}{\partial x} = \frac{\sigma}{E} = \frac{P}{AE}$, therefore:

$$\frac{\partial}{\partial x}\frac{\partial u}{\partial x} = \frac{\partial}{\partial x}\frac{P}{AE} = \frac{\partial^2 u}{\partial x^2} = \frac{1}{AE}\frac{\partial P}{\partial x} \tag{4.3}$$

and substituting 4.3 into 4.2 with mass $m = \rho A dx$ and wave speed $c = \sqrt{\frac{E}{\rho}}$, the wave equation is derived:

$$\frac{\partial^2 u}{\partial x^2} = \left(\frac{1}{c^2}\frac{\partial^2 u}{\partial t^2}\right) \tag{4.4}$$

which can be solved using separation of variables. Substituting $u(x,t) = X(x)T(t)$ gives:

$$\frac{1}{X(x)}\frac{\partial^2 X(x)}{\partial x^2} = \frac{1}{c^2}\frac{1}{T(t)}\frac{\partial^2 T(t)}{\partial t^2} \tag{4.5}$$

In order for 4.5 to be valid, both sides of the equation must be equal to a constant. Picking the constant to be $-\left(\frac{\omega}{c}\right)^2$ and separating left and right-hand sides into separate equations in x and t leads to:

$$\frac{\partial^2 X(x)}{\partial x^2} + \left(\frac{\omega}{c}\right)^2 X(x) = 0 \tag{4.6}$$

and

$$\frac{\partial^2 T(t)}{\partial t^2} + \omega^2 T(t) = 0 \tag{4.7}$$

which are solvable using sinusoidal assumed solutions:

$$X(x) = A\sin\left(\frac{\omega}{c}\right)x + B\cos\left(\frac{\omega}{c}\right)x \tag{4.8}$$

and

$$T(t) = C\sin\omega t + D\cos\omega t \tag{4.9}$$

Where constants A and B depend on boundary conditions and C and D on initial conditions. The complete solution to the free-free beam wave equation is therefore:

$$u(x,t) = \left(A\sin\left(\frac{\omega}{c}\right)x + B\cos\left(\frac{\omega}{c}\right)x\right)(C\sin\omega t + D\cos\omega t) \tag{4.10}$$

Next, in order to apply the above derivation to this specific problem, the boundary conditions of zero strain $\frac{\partial u}{\partial x} = 0$ at both free ends of the beam can be applied. First, the derivative of $u(x,t)$ with respect to x is:

$$\frac{\partial u}{\partial x} = \left(A\left(\frac{\omega}{c}\right)\cos\left(\frac{\omega}{c}\right)x - B\left(\frac{\omega}{c}\right)\sin\left(\frac{\omega}{c}\right)x\right)(C\sin\omega t + D\cos\omega t) \tag{4.11}$$

Applying the boundary condition at x = 0:

$$\left(\frac{\partial u}{\partial x}\right)_{x=0} = A\left(\frac{\omega}{c}\right)(C\sin\omega t + D\cos\omega t) = 0 \tag{4.12}$$

And at x = L:

$$\left(\frac{\partial u}{\partial x}\right)_{x=L} = \left(\frac{\omega}{c}\right)\left(-B\sin\left(\frac{\omega L}{c}\right)\right)(C\sin\omega t + D\cos\omega t) = 0 \tag{4.13}$$

Equation 4.12 implies that A = 0, and since the solution would be trivial if B = 0 in 4.13, $\sin\frac{\omega L}{c} = 0$ instead. This implies that $\frac{\omega L}{c} = \pi, 2\pi ... n\pi$, which can be written succinctly as the natural frequency equation ω_n:

$$\omega_n = \left(\frac{n\pi}{L}\right)\sqrt{\frac{E}{\rho}} \tag{4.14}$$

This equation closely matched an FEA eigenfrequency analysis and experimental results, leading to confidence in its accuracy for the devices in question.

Considering equation 4.10 with zero initial displacement, $u(x,0) = 0$, implies that D = 0. There were four unknowns to begin with (A, B, C, D), and two were eliminated (A and D), leaving two still undetermined. For now we can combine these two remaining constants and create a new constant from their product: $BC = A'$. Thus the generic mode shapes of the free-free beam under axial loading are:

$$u_n = A' \cos\left(\frac{n\pi}{L}\right) x \sin\left(\frac{n\pi}{L}\right)\left(\sqrt{\frac{E}{\rho}}\right) t \tag{4.15}$$

Utilizing the modal results above, predicted gain can be evaluated analytically through the use of the linear equations of piezoelectricity [46]. In order to design the electrodes, numeric and analytic models were used to predict the electrode coverage that would provide highest gain. For a 1.25mm x 10mm geometry (equal in volume to the 4mm diameter devices described in Chapter 3), electrode coverage was simulated from two extremes: a pair of short outer electrodes covering a small area combined with a single long inner electrode covering the majority of the device, to the converse, long outer electrodes with a short inner electrode (see figure 4.2). The design was also evaluated with input and output positions switched, meaning that the two outer electrodes acted as the input, with the inner electrode acting as the output, but lower gain was predicted. The purpose of this was to test whether the

two locations at the edges (experiencing maximum strain) or the single location at the center of the device (experiencing maximum stress) were preferable for achieving maximum output voltage. The latter arrangement, with maximum stress at the center of the device providing output voltage at a central electrode, was preferable.

Figure 4.2 shows that when comparing numeric and FEA models of inner output electrode configuration free-free beam devices, the highest gain is predicted to occur between 60-70% coverage of the device by the input electrodes, which acted as a design guide for device microfabrication. Tethers were designed to be as as short and narrow as possible, to minimize device footprint, while still supporting device mass during fabrication and testing.

4.4 Results

4.4.1 Microfabrication Results

Figure 4.3 shows microfabrication results for free-free beam transformers fabricated with the process described in section 2.1. Following modeling results, input electrodes were designed to cover roughly 65% of device area, surrounding an output electrode. Fabricated devices span 3 orders of magnitude by volume (largest devices are equivalent in volume to 4mm diameter disc transformers). Zoomed optical and SEM images can be seen in figures: 4.4, 4.5, 4.6, 4.7.

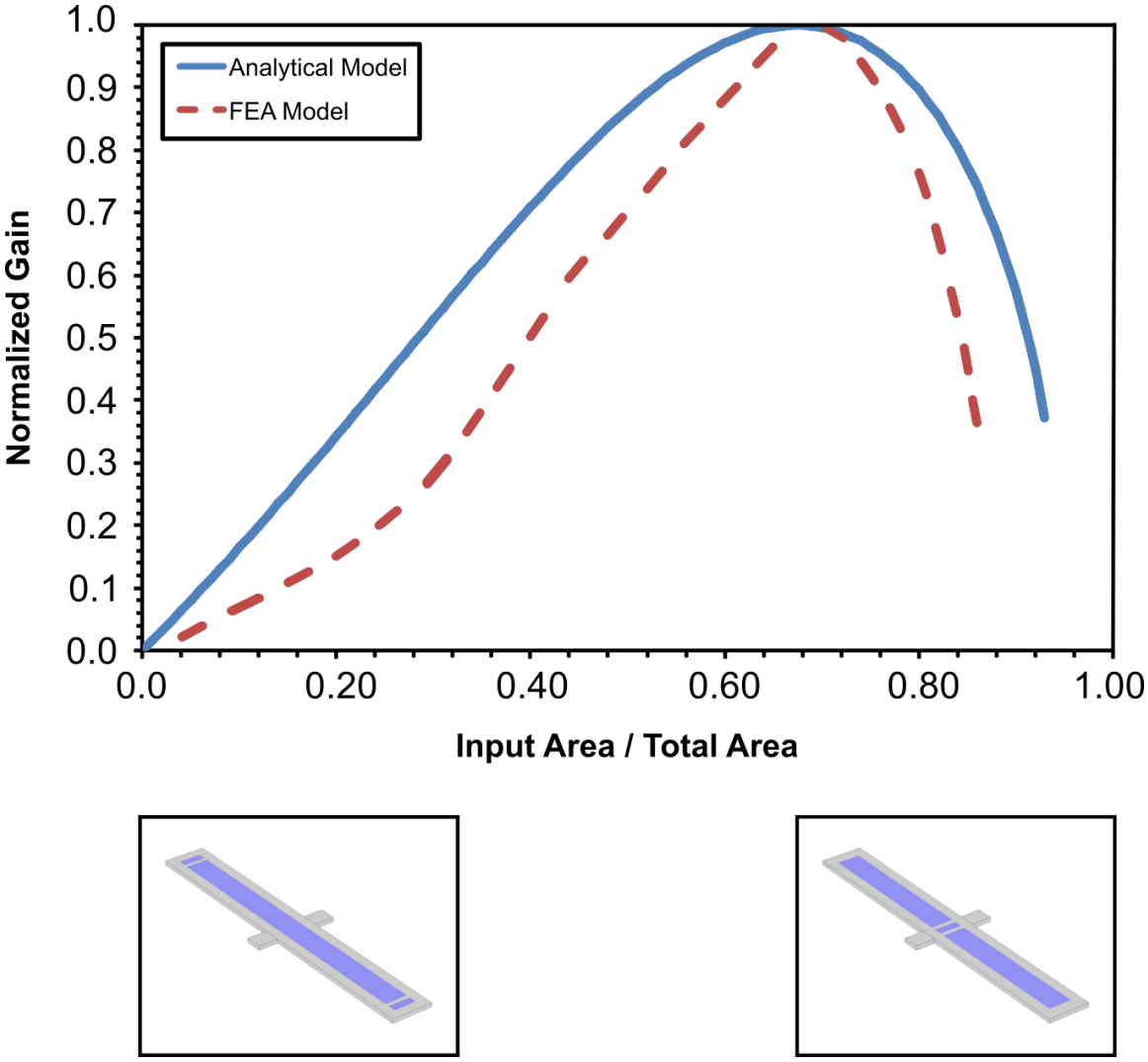

Figure 4.2: FEA (solid line) and analytical (dashed line) predictions of gain vs. electrode topology with output taken from center electrode. Both models predicted maximum gain to occur between 60-70% input electrode coverage of the device, which acted as a guide during device design.

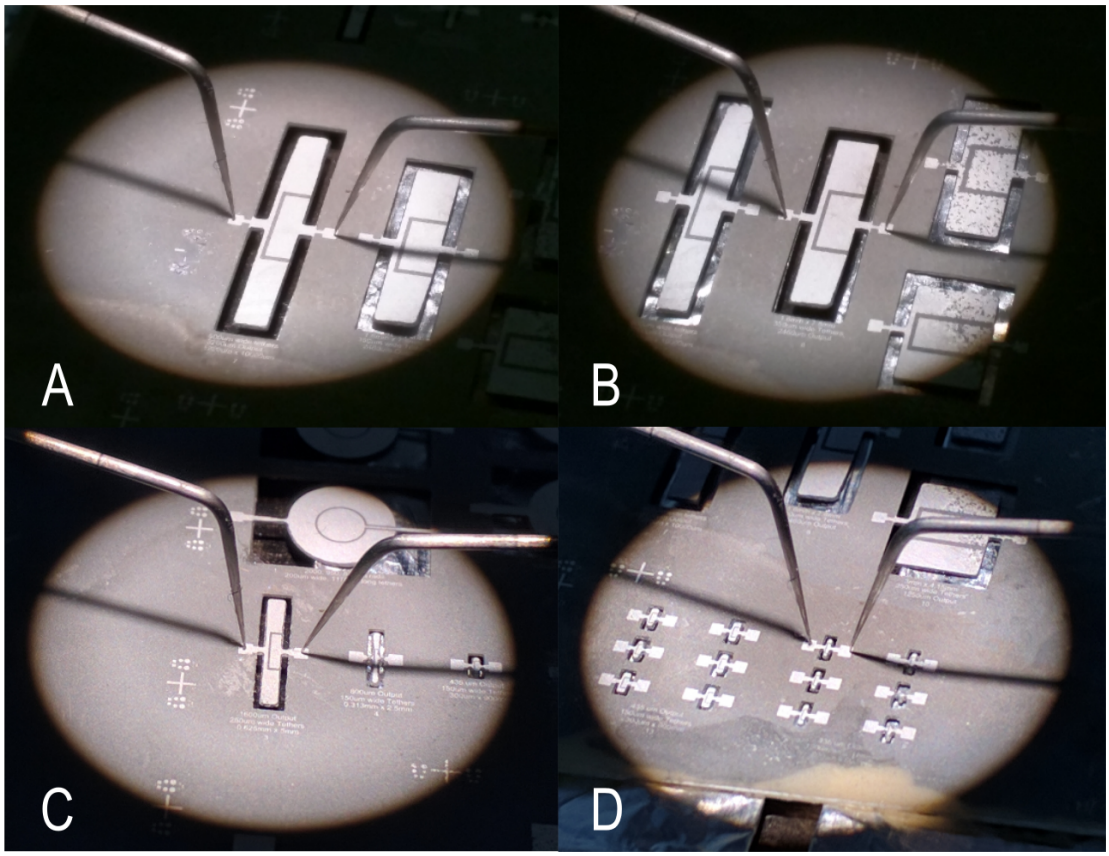

Figure 4.3: Microfabrication results for free-free beam piezoelectric transformers across 3 orders of magnitude in size: (A) 1.3mm x 10.0mm with 500μm wide tethers; (B) 1.6mm x 7.8mm with 350μm wide tethers; (C) 625μm x 5.0mm with 250μm wide tethers; (D) 200/300μm x 900μm with 150μm wide tethers (scale: light circle diameter = 1.6cm)

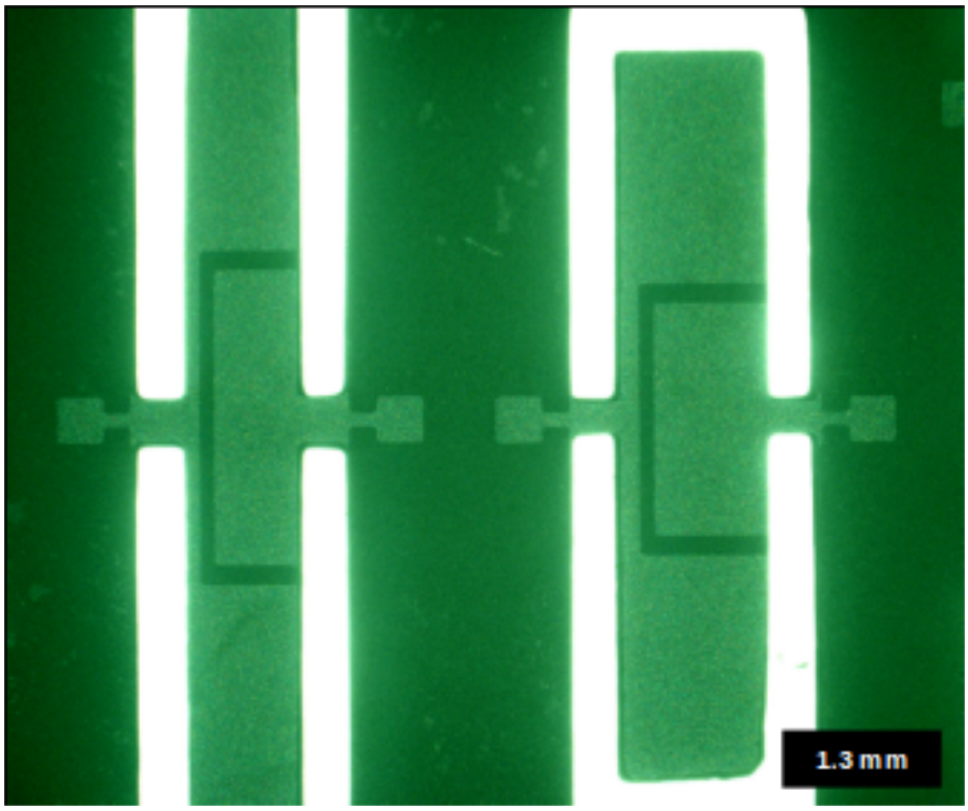

Figure 4.4: Optical image of 1.3mm x 10.0mm (left) and 1.6mm x 7.8mm (right) transformers. 1.3mm x 10.0mm device achieved resonance at 154kHz, with Q = 51; 1.6mm x 7.8mm device at 193kHz, with Q = 33.

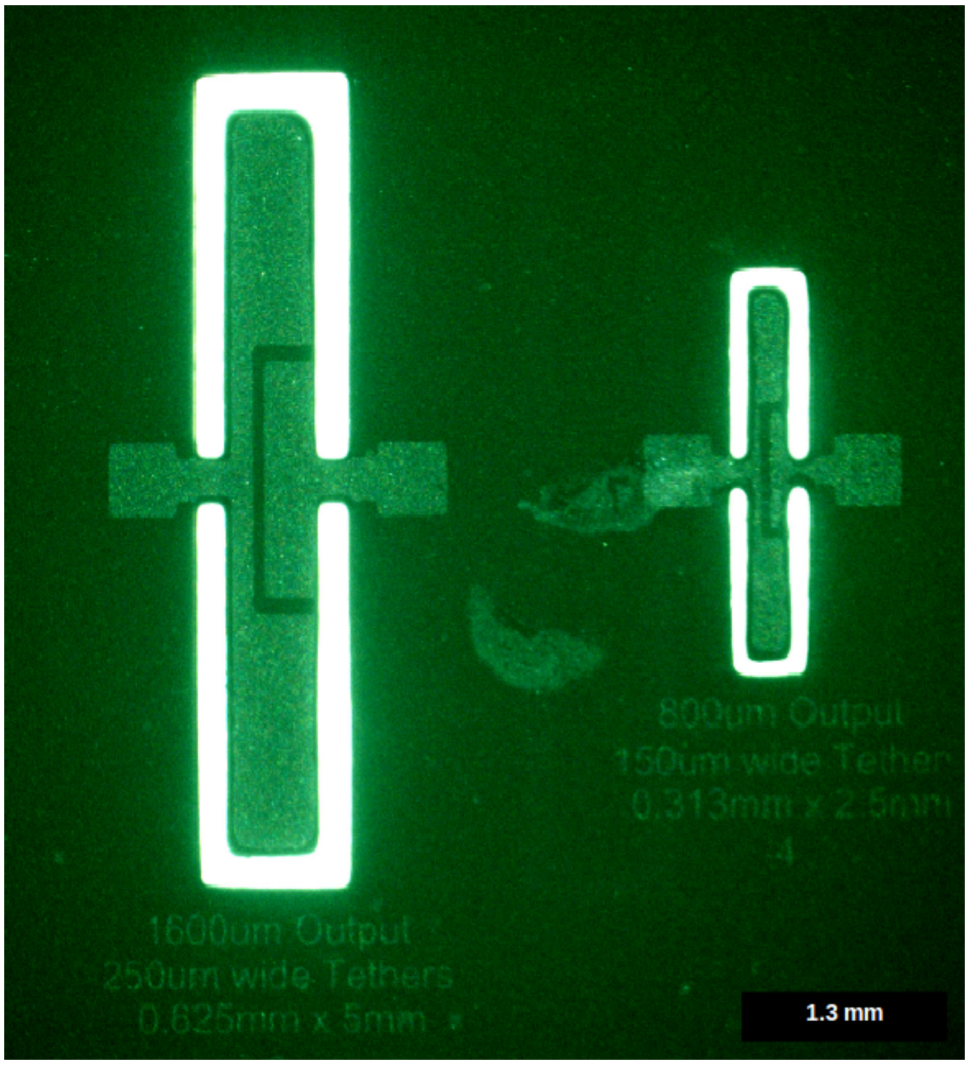

Figure 4.5: Optical image of 625μm x 5.0mm (left) and 313μm x 2.5mm (right) devices. 625μm x 5.0mm device achieved resonance at 295kHz, with Q = 44; 313μm x 2.5mm device did not achieve resonance.

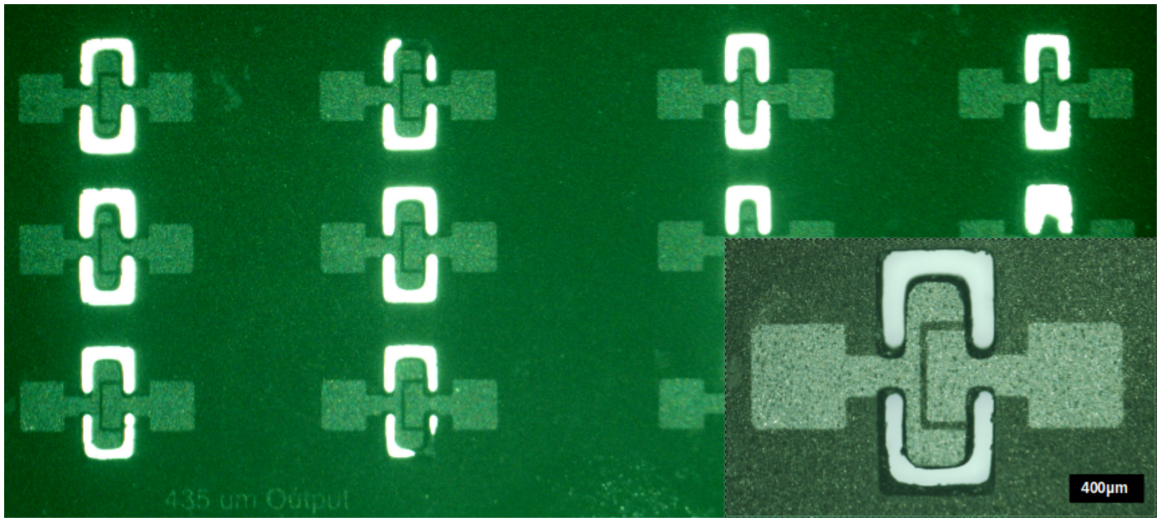

Figure 4.6: Optical image of $300\mu m$ x $900\mu m$ (left) and $200\mu m$ x $900\mu m$ (right) devices; these devices did not achieve resonance, as discussed in this chapter.

4.4.2 Device Performance Results

The performance of the devices that achieved resonance is documented in figures 4.8 and 4.9. The two larger devices (154kHz and 193kHz) achieved maximum gain of roughly 1.2 at 1MΩ output resistance, with efficiencies of 15-20%. The smaller 295kHz device achieved less than unity gain at 1MΩ, while operating at 45% efficiency. Free-free beam device performance was similar to that of the circular disc devices, in that gain increased with increasing electrical load, as expected. The largest devices achieved over unity gain, but only roughly half the maximum gain performance of circular devices was realized. The main cause for the reduced gain is likely due to reaching the limits of the present microfabrication process. Peak efficiency was 20% higher for free-free beam devices when compared to disc devices,

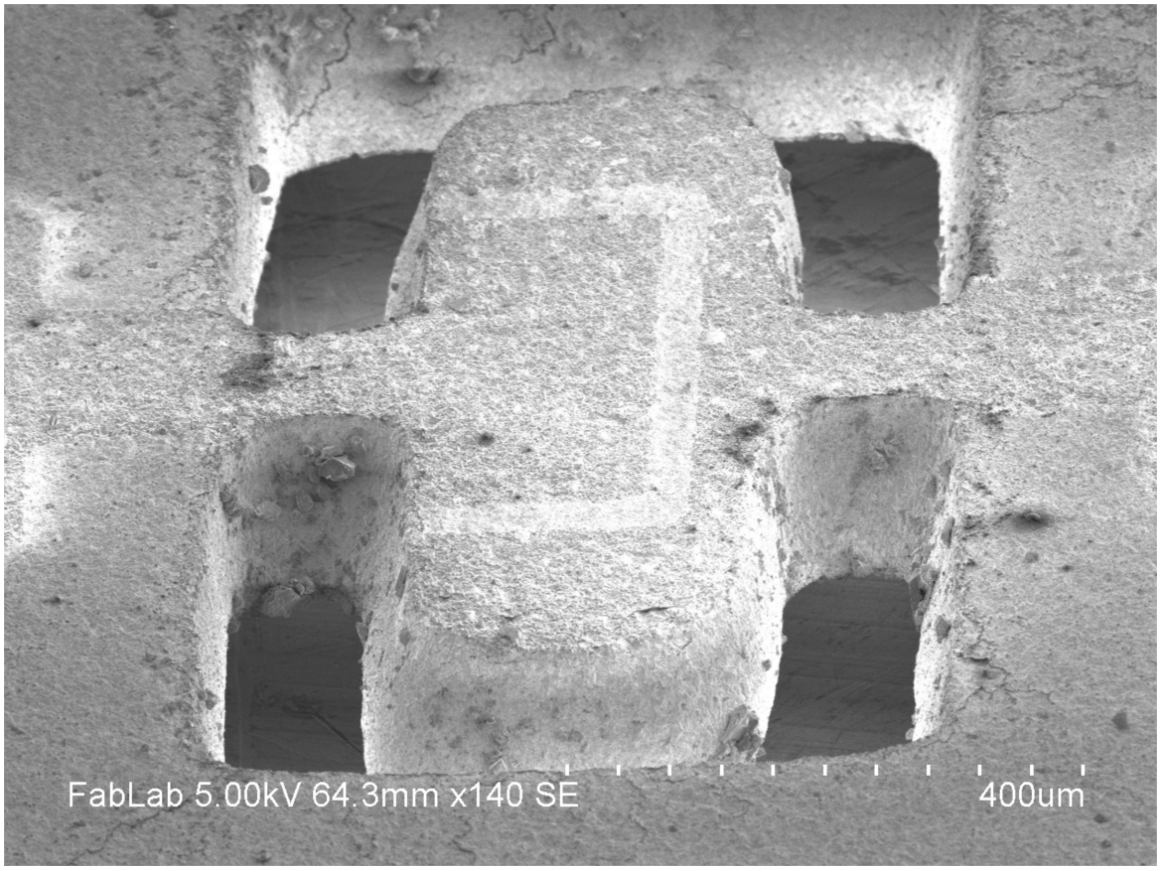

Figure 4.7: SEM image of $300\mu m$ x $900\mu m$ device, demonstrating that the device was fully released with good powderblasting resolution.

in line with expectations for greater efficiency, due to tethering attachment points being located at central node locations.

Free-free beam devices were successfully fabricated and tested across multiple size scales, and by tethering the devices at their central node locations, the effect on device performance was minimized when compared with the circular disc device tethers which constrained radial disc motion during device operation. Device performance was degraded by the microfabrication challenges described in section 2.1, which damaged sections of the devices within 300μm of the edges around powderblasted regions. With an improved microfabrication process, such as one currently being developed by another student in our group, Prakruthi Hareesh, these challenges can hopefully be overcome, leading to free-free beam devices with gain closer to that of the present circular disc devices, and potentially improved efficiency.

A review of current literature yielded no similar bulk devices. Compared to similar (but smaller by volume) thin-film devices [38], the present devices are easier to fabricate, but cannot achieve the same peak levels of efficiency or overall device volume. However, the higher gain achieved in the thin-film devices (5.7) comes at a cost of $<5\%$ efficiency, while the high efficient (60%) operating point is located at 150Ω load, potentially too small for impedance matching with other electronic components in certain applications. Overall, these different devices could be better suited to different applications, and direct comparison is not easy between thin-film and bulk devices.

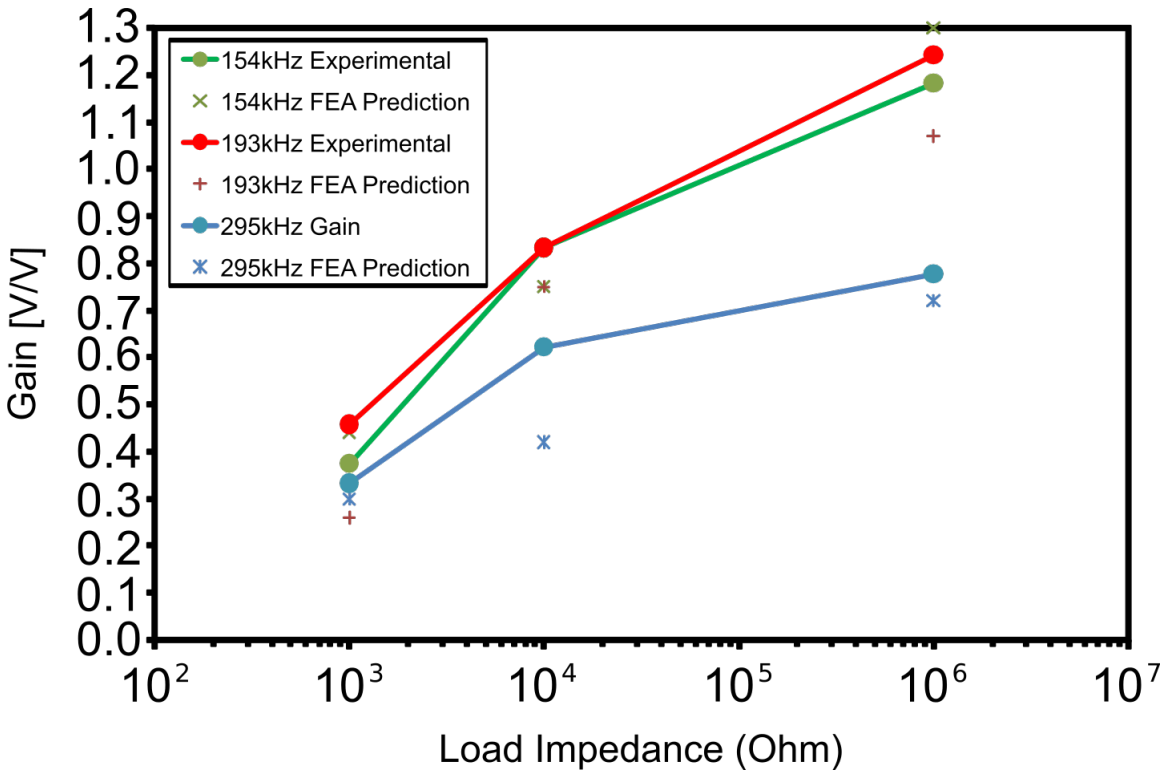

Figure 4.8: Experimental gain results compared to predictive FEA results for free-free beam devices: 154kHz (1.3mm x 10.0mm); 193 kHz (1.6mm x 7.8mm); 295kHz (625μm x 5.0mm). As was the case with circular devices, gain increased with increasing electrical load, and the largest devices achieved over unity gain, but only roughly half the maximum gain performance of circular devices was realized. This is likely due to reaching the limits of the present microfabrication process, as discussed in this section. Lines are added to guide the eye (n=3 trials from a single device in each data set).

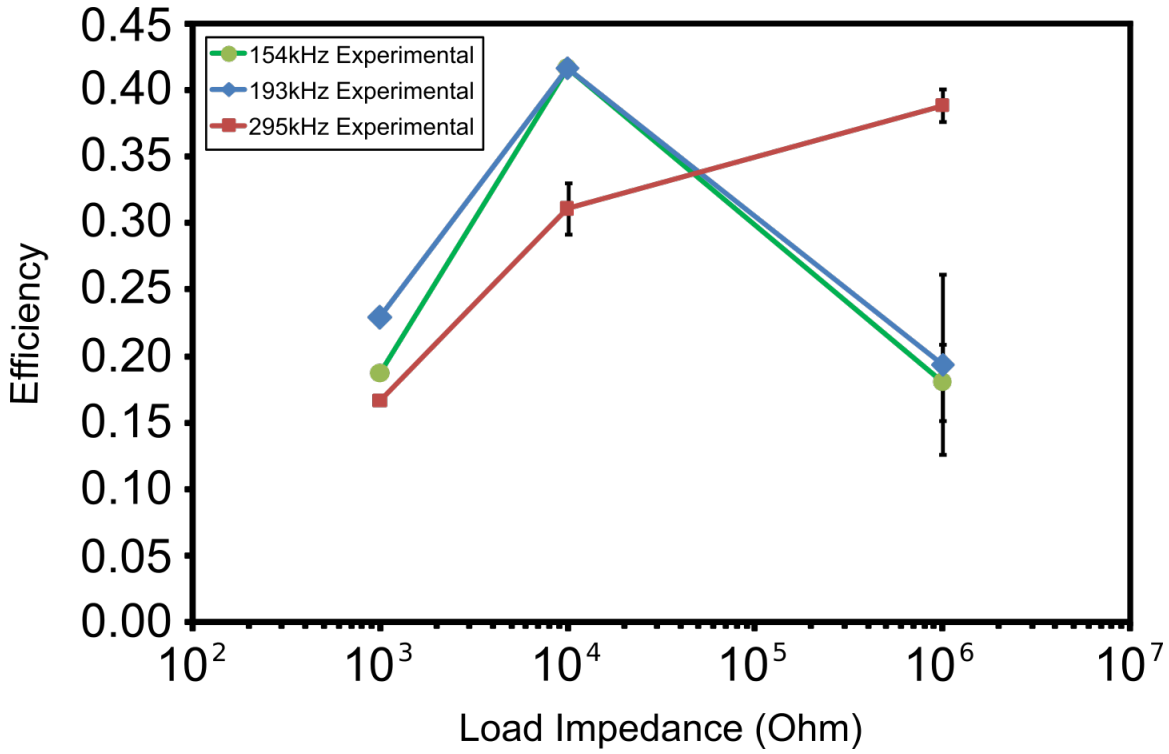

Figure 4.9: Experimental efficiency results for free-free beam devices: 154kHz (1.3mm x 10.0mm); 193 kHz (1.6mm x 7.8mm); 295kHz (625μm x 5.0mm). Maximum efficiency of larger devices at 10kΩ load was higher than that of 4mm diameter circular disc devices, as expected, due to tethering locations being at the device central node location, as opposed to circular devices which were constrained at their outer edge, the location of greatest deflection. The relationship between efficiency and load impedance is impacted by device output impedance, higher for the smaller device (295kHz) than for larger devices. Lines are added to guide the eye (n=3 trials from a single device in each data set).

Chapter 5: Conclusion

In this work, piezoelectric voltage transformers (PTs), intended for micro-robotic or other small-scale electronic or electro-mechanical applications, were investigated. At the outset of the investigation, it wasn't immediately clear whether piezoelectric transformers should be preferable to the main competing technology, electromagnetic transformers (EMTs), or even how they might be compared on quantitative terms, given similar values of voltage gain and efficiency. To that end, power and energy density, volume, and efficiency comparisons were made between prototype devices from the literature. One comparison utilized a Ragone chart contrasting devices on the basis of power and energy density, which demonstrated that prototype PTs in the literature trend towards higher values of power and energy density, compared to EMTs. Since micro-system designers require small, lightweight components, they would prefer technologies that follow such a trend, all else being equal. Therefore, continued development of PTs could see them outpacing EMTs for such applications.

Circular 4mm diameter tethered disc PTs on the order of .002cm^3, at least two orders smaller than the bulk PT literature, were fabricated using photolithography and micropowder blasting. Micropowder blasting is advantageous compared

to other etching techniques because of its speed and relative accuracy. After mask creation and bulk material acquisition, prototype devices in this work could be microfabricated on the order of hours or days, as opposed to weeks for competing thin-film microdevice technologies. Analytical modeling using the Extended Hamilton Method allowed for an investigation into the effects of folded beam tethering on the system performance, predicting an optimal stiffness point in between extreme high and low stiffness values that degraded performance due to overly stiff, or compliant (but massive) tethers, respectively. The as-fabricated folded-beam tethers had predicted stiffness values of 232kN m^{-1}, showing that they are close to optimal theoretical stiffness for a folded flexure design, based on theoretical modeling. Untethered disc transformers were also fabricated to investigate the effect of tethering on device performance, and these devices showed significantly higher gain than tethered designs, as expected, providing evidence that greater device performance could be achieved with improved tethering schemes.

A disc transformer prototype with electrode area ratio = 1 had peak gain of 2.3 ($\pm$ 0.1), efficiency of 33 ($\pm$ 0.1)% and output power density of 51.3 ($\pm$ 4.0)W cm^{-3} (for output power of 80 ($\pm$ 6)mW) at 1MΩ load ($\pm$ one standard deviation). This device exhibits gain similar to some much larger bulk disc devices in the literature, but at lower efficiency. The fact that greater than unity gain is achievable in such small bulk devices is potentially useful to microsystem designers, but efficiency needs to be improved. Tethering disc PTs at their periphery, the location of greatest movement during fundamental radial extension, degrades performance, and changes in tether design or creative microfabrication solutions to provide tethering

at a different location could help improve performance. For example, fundamental resonance modes have a node location at the center of the device, and devising a method to constrain devices at this location could boost performance.

Rectangular topology, free-free beam devices were also fabricated across 3 orders of scale by volume, with the smallest device on the order of .000023cm^3. These devices showed higher quality factors and efficiencies, in some cases, compared to 4mm diameter circular devices, but lower gain (by roughly $\frac{1}{2}$) for equivalent device volume. When comparing these two topologies, the free-free beam devices have the advantage of being easier to fabricate, achieving higher quality factors due to being tethered at node locations, but also having lower gain. In addition, the smallest micro-scale devices (.000023cm^3 volume) did not achieve resonance (did not behave as voltage transformers), as discussed below.

Overall, device performance trends were predicted accurately by analytic and FEA models, but there were areas where accuracy could be improved. Discrepancy between model predictions and experimental device performance could be due to material properties (those used in the models did not match those of the material purchased, due to unavailability of the exact material model from the manufacturer), assumptions made during model generation and, potentially, nonlinear behavior not captured by the linear theory of piezoelectricity. Overall, analytic and FEA models proved to be good analysis tools, and the Extended Hamilton Approach applied here could be used generally in other piezoelectric applications unrelated to voltage transformation.

All of the devices in the present work were affected by an issue with the

fabrication process described here, which was discovered by another student in our research group, Prakruthi Hareesh, while working on a separate project involving micropowder blasting. This issue caused the outer 300μm of each device to become damaged and lose piezoelectric coupling properties. As of this writing, Prakruthi is developing an improved microfabrication process to address this issue. In the present work, the lower limit of the described fabrication process has been found, and simulation models were modified to take into consideration a 300μm zone of material without piezoelectric coupling at the periphery of each device. Hopefully the performance of all future devices will improve with the use of an improved fabrication process, especially the smallest free-free beam devices from the present work that were not operational.

Overall, these devices show promise for integration into small-scale engineered systems, but work needs to be done to improve efficiency (and potentially voltage gain, depending on the application). Macro scale piezoelectric transformers achieve between 80% - 99% efficiency, and for the micro devices in this work to be considered in small-scale systems, their efficiency should be improved. Based on analytical modeling and results comparing different types of tethered devices with untethered ones, improved tethering schemes could improve performance of radial designs, and improved microfabrication techniques should improve the performance of all devices presented here.

5.1 Future Work

In order to move bulk PT technology forward at mm and μm scales, the following areas can be further investigated: materials; device topologies; microfabrication methods.

The present work considered one type of material, PZT-5A, which can be considered soft, meaning it has a relatively low quality factor, but relatively high piezoelectric coefficients. Other materials are available, including hard materials with much higher (more than 10x) quality factors, at the expense of lower piezoelectric coefficients. Also, a newer subset of piezoelectric materials called "relaxor" ferroelectrics (also known as "single-crystal" piezoelectric materials, or ferroelectric materials that exhibit high electrostriction) are becoming available from a few vendors, at high cost. These materials are worth considering due to their extremely high piezoelectric coefficients, 5-10x higher than any other traditional material on the market at this time. The prediction of PT device performance is difficult, due to the combination of electro-mechanical properties that come into play, so an experimental analysis comparing different materials, supplemented by predictive simulations, may be a good place to start in this area.

The present work considered two types of device topologies, circular discs and free-free cantilever beams, but others have been reported in the bulk device literature. The most prevalent macro-scale topology, Rosen bar-type, was not considered because of difficulties in microfabricating this topology with traditional microsystem processes. If this topology could be implemented at the micro scale, through

the use of creative fabrication techniques, higher gain values could potentially be realized.

Finally, future innovative applications of small-scale PTs could include sensors for biological applications. PTs are resonant devices, and their resonant behavior would be altered by the addition of mass on device surfaces, similar to surface acoustic wave devices or resonant beam sensors. PTs already integrated into systems and performing voltage transformation functions could potentially serve dual-purpose roles within the system as sensors, reducing the total sensor count needed for a given application.

Appendix A: Matlab Code

Please see my website for downloadable versions of the numeric models in this work:

www.olivermbarham.com/academia/

```
%% 4 mm diameter untethered (ideal) disc PT model
% Based on my derivation and Rogacheva "The Theory of Piezoelectric Shells and Pla
% Oliver M. Barham, 2017
clc;clear all;close all;
%% Device Geometry & Model Inputs
N = 1000; %number of points
Rb = 2000e-6; %disc outer radius [m]
Ra = 1060e-6; %inner radius (no-gap assumption) (vary this value to get desired ar
RaRb_ratio = round(N*(Ra/Rb)); %used for interrogating model to edge of output ele
t = 127e-6; %thickness [m]
output_area = pi*Ra^2; %[m^2]
V_in = 5; %input voltage [V]
Qd = 30; %quality factor related to damping, experimental value
```

```
lf = 1/Qd; %isotropic loss factor

%% Piezo Material Constants {PZT-5 from Rogacheva}

s_11 = 16.4e-12*(1-1i*lf);s_12 = -5.74e-12*(1-1i*lf); %compliance [1/Pa]

nu = -s_12/s_11;%poisson

rho = 7750; %density [kg/m^3]

epsilon_T = 1700*(8.85e-12)*(1-1i*.066); % [F/m]

d_31 = -172e-12; % [m/V] or [C/N]

k_31_sqd = d_31^2/(s_11*epsilon_T);

k_p_sqd = 2 * k_31_sqd / (1-nu);

B = (2 - (1-nu)*k_p_sqd) / (2*s_11*(1-nu^2)*(1 - k_p_sqd));

sigma = (2*nu + (1-nu)*k_p_sqd) / (2 - (1-nu)*k_p_sqd);

%% Resonance Frequency Prediction:

LR=2.38; %Nondimensional fundamental frequency

lambda = (LR / (Rb)); %[1/m]

omega = abs(sqrt(lambda^2 / (rho*s_11*(1-nu^2)))); %[rad/s] Eq 30.6, pg. 121

omega_kHz = round(omega/(2*pi*1e3))

%[kHz] matches experimental = 567 kHz

%% Deflection Model

step_size = Rb/N;

r = linspace(eps,Rb,N); %extents of coordinate r

r_a = linspace(eps,Ra,N/2); %radius coordinate from zero to Ra [m]

r_b = linspace(Ra+step_size,Rb,N/2); %radius coordinate from Ra to Rb [m]

%Approach Based on Rogacheva eqn. 30.22 + 30.24, for partially electroded disc
```

```
% Determine "C" constants, pg. 127:

eta = sqrt( (rho*omega^2) / B);

a_11 = besselj(1,eta*Ra);

a_12 = -besselj(1,lambda*Ra);a_13 = -bessely(1,lambda*Ra);

a_21 = B * s_11 * (eta*besselj(0,eta*Ra) - ((1-sigma)/Ra)*besselj(1,eta*Ra));

a_22 = - (1/(1-nu^2)) * (lambda*besselj(0,lambda*Ra) - ((1-nu)/Ra)*besselj(1,lambd

a_23 = - (1/(1-nu^2)) * (lambda*bessely(0,lambda*Ra) - ((1-nu)/Ra)*bessely(1,lambd

a_31=0;

a_32 = (1/(1-nu^2)) * (lambda*besselj(0,lambda*Rb) - ((1-nu)/Rb)*besselj(1,lambda*

a_33 = (1/(1-nu^2)) * (lambda*bessely(0,lambda*Rb) - ((1-nu)/Rb)*bessely(1,lambda*

b_1 = 0;

b_2 = (d_31/(1-nu))*(V_in/t);

b_3 = -(d_31/(1-nu))*(V_in/t);

a = [a_11 a_12 a_13;a_21 a_22 a_23;a_31 a_32 a_33];

b = [b_1;b_2;b_3];

C = inv(a)*b;

C_1 = C(1);C_2 = C(2);C_3 = C(3);

u_r_a = C_1 * besselj(1,eta*r_a);

%without electrodes

u_r_b = C_2 * besselj(1,lambda*r_b) + C_3 * bessely(1,lambda*r_b); %with electrode

u_r = abs([u_r_a u_r_b]);

figure(1);plot((r/Rb),(u_r/max(u_r)));title('AR4 Disc Transformer Radial Deflectio

(No Tethers)');
```

```
xlabel('r/Rb');ylabel('u_r [normalized]');

%% Voltage Output Model, Based on Deflection Model

% First derivative of deflection

u_r_dr = ( diff([eps; u_r(:)])./diff([eps; r(:)]) )';

V_out = zeros(RaRb_ratio,RaRb_ratio);

iter=0;

RL_a = linspace(1,1e4,300);

RL_b = linspace(1.1e4,1e6,RaRb_ratio-300);

RL_plot = [RL_a RL_b];

for RL = RL_plot

iter = iter+1;

V_out(iter,:) = ((d_31*RL*omega*output_area)/(s_11*(1-nu))) .* (r(1:RaRb_ratio) .*

u_r_dr(1:RaRb_ratio) + u_r(1:RaRb_ratio))*1i ./ ...

( r(1:RaRb_ratio)*1i + r(1:RaRb_ratio) * ((epsilon_T * RL * omega *output_area)/t)

end

for kk = 1:1:RaRb_ratio;V_out_mean(kk) = mean(abs(V_out(kk,2:end)));

end

% Experimental Data

AR4_RL_data_x = [1.50E+01 6.70E+02 1.00E+03 4.60E+03 1.00E+04 1.77E+04 2.72E+04

4.95E+04...

9.90E+04 1.98E+05 5.00E+05 1.00E+06];

% No tethers:

AR4_RL_data_y1 = [0.32 0.79 1.49 2.32 3.61 4.17 4.25 4.44 4.60 4.63 4.67 4.70];
```

```
% With tethers:
AR4_RL_data_y2 = [0.28 1.13 1.33 1.99 2.16 2.19 2.18 2.23 2.25 2.26 2.23 2.25];
figure(2);semilogx(RL_plot,V_out_mean/V_in,'--');xlabel('Electrical Load [Ohm]','f
ylabel('Gain [V/V]','fontsize',12);...
title('Gain vs. Electrical Load for 4mm Diameter Disc Transformer (No Tethers)','f
semilogx(AR4_RL_data_x,AR4_RL_data_y1,'o');
semilogx(AR4_RL_data_x,AR4_RL_data_y2,'+');
legend('Analytical Model','Experimental: No Tethers','Experimental: Tethers','Loca
%
save XXXX.txt varname -ASCII
```

Bibliography

[1] W W Shao, L J Chen, C L Pan, Y B Liu, and Z H Feng. Power density of piezoelectric transformers improved using a contact heat transfer structure. *IEEE Trans Ultrason Ferroelectr Freq Control*, 59(1):73–81, 2012.

[2] Manh Cuong Do. *Piezoelectric Transformer Integration Possibility in High Power Density Applications*. PhD thesis, TECHNISCHE UNIVERSITAT DRESDEN, 2008.

[3] Shashank Priya, Seyit Ural, Hyeoung Woo Kim, Kenji Uchino, and Toru Ezaki. Multilayered unipoled piezoelectric transformers. *Japanese Journal of Applied Physics, Part 1: Regular Papers and Short Notes and Review Papers*, 43(6 A):3503–3510, 2004.

[4] Yuan Zhuang, Seyit O Ural, Rohan Gosain, Safakcan Tuncdemir, Ahmed Amin, and Kenji Uchino. High Power Piezoelectric Transformers with Pb(Mg1/3Nb2/3)O3PbTiO3Single Crystals. *Applied Physics Express*, 2(12):121402, 2009.

[5] E L Horsley, M P Foster, and D A Stone. State-of-the-art piezoelectric transformer technology. *2007 European Conference on Power Electronics and Applications, Vols 1-10*, pages 1637–1646, 2007.

[6] K J Tseng, J Du, and J Hu. Piezoelectric transformer with high power density and multiple outputs. *Electronics Letters*, 40(12):786–788, 2004.

[7] H L Sun, D M Lin, K H Lam, M S Guo, S H Choy, K W Kwok, and H L W Chan. High power density NaNbO3-LiTaO3 lead-free piezoelectric transformer in radial vibration modes. *Smart Materials and Structures*, 24(6), 2015.

[8] M Katsuno, Y Fuda, and M Tamura. High-power ceramic materials for piezoelectric transformers. *Electronics and Communications in Japan Part Iii-Fundamental Electronic Science*, 82(11):86–92, 1999.

[9] P Laoratanakul, A V Carazo, P Bouchilloux, and K Uchino. Unipoled disk-type piezoelectric transformers. *Japanese Journal of Applied Physics Part 1-Regular Papers Short Notes & Review Papers*, 41(3A):1446–1450, 2002.

[10] J Navas, T Bove, J A Cobos, F Nuno, K Brebol, and Ieee Ieee. Miniaturised battery charger using piezoelectric transformers. In *Apec 2001: Sixteenth Annual Ieee Applied Power Electronics Conference and Exposition, Vols 1 and 2*, pages 492–496, 2001.

[11] Erkan A Gurdal, Seyit O Ural, Hwi-Yeol Park, Sahn Nahm, and Kenji Uchino. High Power (Na0.5K0.5)NbO3-Based Lead-Free Piezoelectric Transformer. *Japanese Journal of Applied Physics*, 50(2):27101, 2011.

[12] Vo Viet Thang, In-Sung Kim, Soon-Jong Jeong, Min-Soo Kim, and Jae-Sung Song. Modeling and Investigation of Multilayer Piezoelectric Transformer with a Central Hole for Heat Dissipation. *Journal of Electrical Engineering and Technology*, 6(5):671–676, 2011.

[13] O Ohnishi, H Kishie, A Iwamoto, Y Sasaki, T Zaitsu, and T Inoue. Piezoelectric Ceramic Transformer Operating in Thickness Extensional Vibration Mode for Power-Supply. *Ieee 1992 Ultrasonics Symposium : Proceedings, Vols 1 and 2*, pages 483–488, 1992.

[14] P J M Smidt, J L Duarte, and Ieee. Powering neon lamps through piezoelectric transformers. In *Pesc 96 Record - 27th Annual Ieee Power Electronics Specialists Conference, Vols I and Ii*, pages 310–315, 1996.

[15] D Vasic, F Costa, and E Sarraute. Piezoelectric transformer for integrated MOSFET and IGBT gate driver. *Ieee Transactions on Power Electronics*, 21(1):56–65, 2006.

[16] S C Tang, S Y Hui, and H S H Chung. Coreless planar printed-circuit-board (PCB) transformers - A fundamental concept for signal and energy transfer. *Ieee Transactions on Power Electronics*, 15(5):931–941, 2000.

[17] C R Sullivan, S R Sanders, and Ieee. Measured performance of a high-power-density microfabricated transformer in a DC-DC converter. In *Pesc 96 Record - 27th Annual Ieee Power Electronics Specialists Conference, Vols I and Ii*, pages 287–294, New York, 1996. I E E E.

[18] Strydom. *Electromagnetic Design of Integrated Resonator-Transformers*. PhD thesis, 2001.

[19] T O'Donnell, N N Wang, M Brunet, S Roy, A Connell, J Power, C O'Mathuna, P McCloskey, and Ieee. Thin film micro-transformers for future power conversion. In *Apec 2004: Nineteenth Annual Ieee Applied Power Electronics Conference and Exposition, Vols 1-3*, pages 939–944, 2004.

[20] M Brunet, T O'Donnell, L Baud, N N Wang, J O'Brien, P McCloskey, and S C O'Mathuna. Electrical performance of microtransformers for DC-DC converter applications. *Ieee Transactions on Magnetics*, 38(5):3174–3176, 2002.

[21] Yichao Tang and Alireza Khaligh. Bidirectional Resonant DC-DC Step-Up Converters for Driving High-Voltage Actuators in Mobile Microrobots. *IEEE Transactions on Power Electronics*, 31(1):340–352, 2016.

[22] J T Strydom and J D van Wyk. Volumetric limits of planar integrated resonant transformers: A 1 MHz case study. *Ieee Transactions on Power Electronics*, 18(1):236–247, 2003.

[23] J B Goodenough and Y Kim. Challenges for Rechargeable Li Batteries. *Chemistry of Materials*, 22(3):587–603, 2010.

[24] A P Chandrakasan, S Sheng, and R W Brodersen. LOW-POWER CMOS DIGITAL DESIGN. *Ieee Journal of Solid-State Circuits*, 27(4):473–484, 1992.

[25] J Yang. Piezoelectric transformer structural modeling–a review. *IEEE Trans Ultrason Ferroelectr Freq Control*, 54(6):1154–1170, 2007.

[26] Frederick Bedell. History of AC wave form, its determination and standardization. *Electrical Engineering*, 61(12):864–868, 1942.

[27] William Stanley. Induction Coil, 1886.

[28] A Morched, L Marti, and J Ottevangers. A HIGH-FREQUENCY TRANSFORMER MODEL FOR THE EMTP. *Ieee Transactions on Power Delivery*, 8(3):1615–1626, 1993.

[29] Keith A Fish, Charles A Rosen, and Herbert C Rothenberg. Electromechanical transducer, 1958.

[30] Jeffrey S Pulskamp, Ronald G Polcawich, Ryan Q Rudy, Sarah S Bedair, Robert M Proie, Tony Ivanov, and Gabriel L Smith. Piezoelectric PZT MEMS technologies for small-scale robotics and RF applications. *MRS Bulletin*, 37(11):1062–1070, 2012.

[31] Seong Kon Kim and Young Ho Seo. Fabrication and characterization of the piezoelectric microtransformer based on microelectromechanical systems. *Applied Physics Letters*, 88(26):263510, 2006.

[32] Michael Karpelson, Gu-Yeon Wei, and Robert J Wood. Driving high voltage piezoelectric actuators in microrobotic applications. *Sensors and Actuators A: Physical*, 176:78–89, 2012.

[33] Brian Morgan, Sarah Bedair, Jeffrey S Pulskamp, Ronald G Polcawich, Christopher Meyer, Christopher Dougherty, Xue Lin, David Arnold, Rizwan Bashirullah, Ryan Miller, and Mark Roosz. Power Considerations for MAST

Platforms. In T George, M S Islam, and A K Dutta, editors, *Micro- and Nanotechnology Sensors, Systems, and Applications Ii*, volume 7679. 2010.

[34] G Ivensky, I Zafrany, and S Ben-Yaakov. Generic operational characteristics of piezoelectric transformers. *Ieee Transactions on Power Electronics*, 17(6):1049–1057, 2002.

[35] I Kartashev and T Vontz. Regimes of piezoelectric transformer operation II. *Measurement Science & Technology*, 20(5):55108, 2009.

[36] P B Koeneman, I J BuschVishniac, and K L Wood. Feasibility of micro power supplies for MEMS. *Journal of Microelectromechanical Systems*, 6(4):355–362, 1997.

[37] F Blaabjerg, M Liserre, and K Ma. Power Electronics Converters for Wind Turbine Systems. *Ieee Transactions on Industry Applications*, 48(2):708–719, 2012.

[38] Sarah S Bedair, Jeffrey S Pulskamp, Ronald G Polcawich, Brian Morgan, Joel L Martin, and Brian Power. Thin-Film Piezoelectric-on-Silicon Resonant Transformers. *Journal of Microelectromechanical Systems*, 22(6):1383–1394, 2013.

[39] Shuo Cheng. THEORY, DESIGN, AND APPLICATION OF ELECTRODYNAMIC TRANSFORMERS. 2011.

[40] Shuo Cheng and David P Arnold. Microfabricated electrodynamic transformers for electromechanical power conversion. *Journal of Micromechanics and Microengineering*, 23(11):114002, 2013.

[41] S Roundy and P K Wright. A piezoelectric vibration based generator for wireless electronics. *Smart Materials & Structures*, 13(5):1131–1142, 2004.

[42] Anita M. Flynn and Seth R. Sanders. Fundamental limits on energy transfer and circuit considerations for piezoelectric transformers. *IEEE Transactions on Power Electronics*, 17(1):8–14, 2002.

[43] D. V. Ragone. Review of Battery Systems for Electrically Powered Vehicles. Technical report, 1968.

[44] Z S Wu, K Parvez, X L Feng, and K Mullen. Graphene-based in-plane micro-supercapacitors with high power and energy densities. *Nature Communications*, 4, 2013.

[45] D Vasic, E Sarraute, F Costa, P Sangouard, and E Cattan. Piezoelectric micro-transformer based on SOI structure. *Sensors and Actuators a-Physical*, 117(2):317–324, 2005.

[46] A H Meitzler, H F Tiersten, A W Warner, D Berlincourt, G A Couqin, and F S Welsh III. IEEE standard on piezoelectricity ANSI/IEEE Std 176-1987. Technical report, American National Standards Institute, New York, 1988.

[47] T Sebastian, L Kozielski, and J Erhart. Co-sintered PZT ceramics for the piezoelectric transformers. *Ceramics International*, 41(8):9321–9327, 2015.

[48] Xiaolian Chao, Zupei Yang, Gang Li, and Yaoqiang Cheng. Fabrication and characterization of low temperature sintering PMNPZNPZT step-down multilayer piezoelectric transformer. *Sensors and Actuators A: Physical*, 144(1):117–123, 2008.

[49] Ce-Wen Nan, M I Bichurin, Shuxiang Dong, D Viehland, and G Srinivasan. Multiferroic magnetoelectric composites: Historical perspective, status, and future directions. *Journal of Applied Physics*, 103(3):31101, 2008.

[50] W Eerenstein, N D Mathur, and J F Scott. Multiferroic and magnetoelectric materials. *Nature*, 442(7104):759–765, 2006.

[51] E K Akdogan, M Allahverdi, and A Safari. Piezoelectric composites for sensor and actuator applications. *IEEE Trans Ultrason Ferroelectr Freq Control*, 52(5):746–775, 2005.

[52] J Fan, W A Stoll, and C S Lynch. Nonlinear constitutive behavior of soft and hard PZT: Experiments and modeling. *Acta Materialia*, 47(17):4415–4425, 1999.

[53] Qiming M Zhang and Jianzhong Zhao. Electromechanical properties of lead zirconate titanate piezoceramics under the influence of mechanical stresses. *IEEE transactions on ultrasonics, ferroelectrics, and frequency control*, 46(6):1518–1526, 1999.

[54] S Park and Thomas R Shrout. Ultrahigh strain and piezoelectric behavior in relaxor based ferroelectric single crystals. *Journal of Applied Physics*, 82(4), 1997.

[55] L J Bowen, R L Gentilman, H T Pham, D F Fiore, and K W French. INJECTION-MOLDED FINE-SCALE PIEZOELECTRIC COMPOSITE TRANSDUCERS. In M Levy and B R McAvoy, editors, *Ieee 1993 Ultrasonics Symposium Proceedings, Vols 1 and 2*, pages 499–503, New York, 1993. I E E E.

[56] Jürgen Rödel, Wook Jo, Klaus T P Seifert, EvaMaria Anton, Torsten Granzow, and Dragan Damjanovic. Perspective on the Development of Lead-free Piezoceramics. *Journal of the American Ceramic Society*, 92(6):1153–1177, 2009.

[57] M R Yang, S Y Chu, I H Chan, and S L Yang. Disk-type piezoelectric transformer of a Na0.5K0.5NbO3-CuNb2O6 lead-free ceramic for driving T5 fluorescent lamp. *Journal of Alloys and Compounds*, 522:3–8, 2012.

[58] M Guo, D M Lin, K H Lam, S Wang, H L Chan, and X Z Zhao. A lead-free piezoelectric transformer in radial vibration modes. *Rev Sci Instrum*, 78(3):35102, 2007.

[59] Zhang. Piezoelectric properties in perovskite 0.948 (K 0.5 Na 0.5) Nb O 3 0.052 Li Sb O 3 lead-free ceramics. 2006.

[60] W F Liu and X B Ren. Large Piezoelectric Effect in Pb-Free Ceramics. *Physical Review Letters*, 103(25), 2009.

[61] W P Mason. ELECTROSTRICTIVE EFFECT IN BARIUM TITANATE CERAMICS. *Physical Review*, 74(9):1134–1147, 1948.

[62] Aditya Rajapurkar. *LOSS MECHANISMS IN PIEZOELECTRIC PZT CERAMICS AND SINGLE CRYSTALS*. PhD thesis, Penn State University, 2008.

[63] Ramaroorthy Ramesh and Nicola A Spaldin. Multiferroics: progress and prospects in thin films. *Nature materials*, 6(1):21–29, 2007.

[64] Susan Trolier-McKinstry and Peter Muralt. Thin film piezoelectrics for MEMS. *Journal of Electroceramics*, 12(1-2):7–17, 2004.

[65] N.N. Rogacheva. *The Theory of Piezoelectric Shells and Plates*. CRC Press, 1994.

[66] D Vasic, F Costa, E Sarraute, and Ieee. A new MOSFET & IGBT gate drive insulated by a piezoelectric transformer. In *Pesc 2001: 32nd Annual Power Electronics Specialists Conference, Vols 1-4, Conference Proceedings*, pages 1479–1484, New York, 2001. Ieee.

[67] S Lineykin, S Ben-Yaakov, and Ieee. Feedback isolation by piezoelectric transformers: Comparison of amplitude to frequency modulation. In *Pesc 04: 2004 Ieee 35th Annual Power Electronics Specialists Conference, Vols 1-6, Conference Proceedings*, pages 1834–1840, 2004.

[68] G Ivensky, S Bronstein, and S Ben-Yaakov. A comparison of piezoelectric transformer AC/DC converters with current doubler and voltage doubler rectifiers. *Ieee Transactions on Power Electronics*, 19(6):1446–1453, 2004.

[69] S Bronstein, G Ivensky, S Ben-Yaakov, and Ieee. Parallel connection of piezoelectric transformers. In *Pesc 04: 2004 Ieee 35th Annual Power Electronics Specialists Conference, Vols 1-6, Conference Proceedings*, pages 1779–1785, New York, 2004. Ieee.

[70] Y M Ye, K W E Cheng, and K Ding. A Novel Method for Connecting Multiple Piezoelectric Transformer Converters and its Circuit Application. *Ieee Transactions on Power Electronics*, 27(4):1926–1935, 2012.

[71] J Erhart. Bulk piezoelectric ceramic transformers. *Advances in Applied Ceramics*, 112(2):91–96, 2013.

[72] Petr Plpán and Jií Erhart. Transformation ratio of ring-dot planar piezoelectric transformer. *Sensors and Actuators A: Physical*, 140(2):215–224, 2007.

[73] F Boukazouha, G Poulin-Vittrant, L P Tran-Huu-Hue, M Bavencoffe, F Boubenider, M Rguiti, and M Lethiecq. A comparison of 1D analytical model and 3D finite element analysis with experiments for a rosen-type piezoelectric transformer. *Ultrasonics*, 60:41–50, 2015.

[74] T Hemsel. Modelling and Analysis of Piezoelectric Transformers. 2003.

[75] K T Chang and C W Lee. Fabrication and characteristics of thin disc piezoelectric transformers based on piezoelectric buzzers with gap circles. *Ultrasonics*, 48(2):91–97, 2008.

[76] J Jason Yao, Charles Chien, Robert Mihailovich, and J Jason Yao. RF MEMS from a device perspective. *J. Micromech. Microeng.*, 2000.

[77] Gianluca Piazza. One and Two Port Piezoelectric Higher Order Contour-Mode MEMS Resonators for Mechanical Signal Processing. 51(December):1596–1608, 2007.

[78] S Tadigadapa and K Mateti. Piezoelectric MEMS sensors: state-of-the-art and perspectives. *Measurement Science and Technology*, 20(9):092001, 2009.

[79] C.T.-C. Nguyen. Frequency-selective MEMS for miniaturized communication devices. *1998 IEEE Aerospace Conference Proceedings (Cat. No.98TH8339)*, 1(8):445–460, 1998.

[80] Clark T C Nguyen. MEMS technology for timing and frequency control. *IEEE Transactions on Ultrasonics, Ferroelectrics, and Frequency Control*, 54(2):251–270, 2007.

[81] Gianluca Piazza, Philip J Stephanou, and Albert P Al Pisano. Piezoelectric Aluminum Nitride Vibrating Contour Mode MEMS Resonators. *J. micorelectromechanical Syst.*, 15(6):1406–1418, 2006.

[82] Chengjie Zuo, Nipun Sinha, and Gianluca Piazza. Very high frequency channel-select MEMS filters based on self-coupled piezoelectric AlN contour-mode resonators. *Sensors and Actuators, A: Physical*, 160(1-2):132–140, 2010.

[83] B P Harrington and R Abdolvand. (R)In-plane acoustic reflectors for reducing effective anchor loss in lateralextensional MEMS resonators. *Journal of Micromechanics and Microengineering*, 21:085021, 2011.

[84] Ray-Lee Lin. *Piezoelectric transformer characterization and application of electronic ballast*. PhD thesis, 2001.

[85] C Supatutkul and Y Laosiritaworn. Finite Element Modeling of Ring-Shaped Piezoelectric Transformer. *Ferroelectrics*, 450(1):99–106, 2013.

[86] H L Li, J H Hu, and H L Chan. Finite element analysis on piezoelectric ring transformer. *IEEE Trans Ultrason Ferroelectr Freq Control*, 51(10):1247–1254, 2004.

[87] T Tsuchiya, Y Kagawa, N Wakatsuki, and H Okamura. Finite element simulation of piezoelectric transformers. *Ieee Transactions on Ultrasonics Ferroelectrics and Frequency Control*, 48(4):872–878, 2001.

[88] Shine Tzong Ho. Modeling of a disk-type piezoelectric transformer. *IEEE Transactions on Ultrasonics, Ferroelectrics, and Frequency Control*, 54(10):2110–2119, 2007.

[89] Mendel Kleiner. *Electroacoustics*. CRC Press, 2013.

[90] Sanghoon Lee, Moojoon Kim, Jungsoon Kim, and Seongyeon Yoo. Equivalent circuit with temperature parameters for piezoelectric sensor under space environment. *IEEE International Ultrasonics Symposium, IUS*, pages 847–850, 2012.

[91] François Pigache and Clément Nadal. Modeling and identification of Rosen-type transformer in nonlinear behavior. *IEEE Transactions on Ultrasonics, Ferroelectrics, and Frequency Control*, 58(12):2562–2570, 2011.

[92] Hairen Wang, Yuantai Hu, and Ji Wang. On the Nonlinear Behavior of a Multilayer Circular Piezoelectric Plate-Like Transformer Operating Near Resonance. *IEEE TRANSACTIONS ON ULTRASONICS, FERROELECTRICS, AND FREQUENCY CONTROL*, 60(4):752–757, 2013.

[93] T. Andersen, M. A E Andersen, O. C. Thomsen, M. P. Foster, and D. A. Stone. Nonlinear effects in piezoelectric transformers explained by thermal-electric model based on a hypothesis of self-heating. *IECON Proceedings (Industrial Electronics Conference)*, pages 596–601, 2012.

[94] Yuantai Hu, Huan Xue, Jiashi Yang, and Qing Jiang. Nonlinear behavior of a piezoelectric power harvester near resonance. *IEEE Transactions on Ultrasonics, Ferroelectrics, and Frequency Control*, 53(7):1387–1391, 2006.

[95] P. Ribeiro and M. Petyt. Nonlinear vibration of plates by the hierarchical finite element and continuation methods. *International Journal of Mechanical Sciences*, 41(4-5):437–459, 1999.

[96] Keisuke Ishii, Norihito Akimoto, Shinjiro Tashirio, and Hideji Igarashi. Influence of load resistance on higher harmonic voltages generated in a piezoelectric transformer. *Japanese Journal of Applied Physics, Part 1: Regular Papers and Short Notes and Review Papers*, 37(9 PART B):5330–5333, 1998.

[97] Hareesh K. R. Kommepalli, Kiron Mateti, Christopher D. Rahn, and Srinivas A. Tadigadapa. Piezoelectric T-Beam Actuators. *Journal of Mechanical Design*, 133(6):061003, 2011.

[98] I Misri, P Hareesh, S Yang, and D L DeVoe. Microfabrication of bulk PZT transducers by dry film photolithography and micro powder blasting. *Journal of Micromechanics and Microengineering*, 22(8):85017, 2012.

[99] J Erhart, P Pulpan, R Dolecek, P Psota, and V Ledl. Disc piezoelectric ceramic transformers. *IEEE Trans Ultrason Ferroelectr Freq Control*, 60(8):1612–1618, 2013.

[100] M. Tang, A.B. Yu, A.Q. Liu, A. Agarwal, S. Aditya, and Z.S. Liu. High isolation X-band MEMS capacitive switches. *Sensors and Actuators A: Physical*, 120(1):241–248, 2005.

[101] G D J Su, S H Hung, D X Jia, and F K Jiang. Serpentine spring corner designs for micro-electro-mechanical systems optical switches with large mirror mass. *Optical Review*, 12(4):339–344, 2005.

[102] Kenji Miyamoto, Tomoya Jomori, Koji Sugano, Osamu Tabata, and Toshiyuki Tsuchiya. Mechanical calibration of MEMS springs with sub-micro-Newton force resolution. *Sensors and Actuators, A: Physical*, 143:136–142, 2008.

[103] A.C. Ugural and S.K. Fenster. *Advanced Strength and Applied Elasticity*. Prentice Hall, 2003.

[104] H F Tiersten. *Linear Piezoelectric Plate Vibrations*. Plenum Press, 1969.

[105] Allen H Meitzler and H F Tiersten. Definition and measurement of radial mode coupling factors in piezoelectric ceramic materials with large variations in Poisson's ratio. *IEEE transactions on sonics and ultrasonics*, (20):233–239, 1973.

[106] P.R HEYLIGER and G RAMIREZ. Free Vibration of Laminated Circular Piezoelectric Plates and Discs. *Journal of Sound and Vibration*, 229(4):935–956, 2000.

[107] C H Huang. Theoretical and experimental vibration analysis for a piezoceramic disk partially covered with electrodes. *Journal of the Acoustical Society of America*, 118(2):751–761, 2005.

[108] Leonard Meirovitch. *Fundamentals of Vibrations*. Waveland Press, 2001.

[109] J.N. Reddy. *Energy Principles and Variational Methods in Applied Mechanics*. John Wiley and Sons, Inc, 2002.

[110] Joab R. Winkler and J. Brian Davies. Elimination of spurious modes in finite element analysis. *Journal of Computational Physics*, 56(1):1–14, 1984.

[111] W.C. Tang. Viscous air damping in laterally driven microresonators. *Proceedings IEEE Micro Electro Mechanical Systems An Investigation of Micro Structures, Sensors, Actuators, Machines and Robotic Systems*, pages 199–204, 1994.

[112] Alex V. Mezheritsky. Elastic, dielectric, and piezoelectric losses in piezoceramics: How it works all together. *IEEE Transactions on Ultrasonics, Ferroelectrics, and Frequency Control*, 51(6):695–707, 2004.

[113] Konji Uchino and Seiji Hirose. Loss mechanisms in piezoelectrics: how to measure different losses separately. *Ultrasonics, Ferroelectrics, and Frequency Control, IEEE Transactions on*, 48(1):307–321, 2001.

[114] Shuyu Lin, Jie Xu, and Hui Cao. Analysis on the Ring-Type Piezoelectric Ceramic Transformer in Radial Vibration. *Ieee Transactions on Power Electronics*, 31(7):5079–5088, 2016.

[115] Sarah S Bedair, J Pulskamp, Brian Morgan, and R Polcawich. Performance model of electrode tailored thin film piezoelectric transformers for high frequency switched mode power supplies. *Proc. Power MEMS*, pages 436–438, 2009.

[116] C. Beards. *Structural Vibration: Analysis and Damping*. 1996.